Gravitational Waves from Newly Born Magnetars

A Search Proposal

Brian McGloughlin

Advisors: Béatrice Bonga and Badri Krishnan

Abstract

All detected gravitational wave events from the very first on September 14th 2015 until the time of writing have been produced from a binary system consisting of either a pair of neutron stars, a pair of black holes or both. Continuous gravitational wave signals from isolated rotating neutron stars on the other hand have never been detected, despite great efforts in doing so, due in part to their unique properties that make them computationally expensive to detect. Specifically, signals of this kind are difficult to detect since they both last a relatively long time and the corresponding number of points in parameter space to search over increase non-linearly with the observation time. Successful detection of such signals would provide us with a deep insight into the interior structure of neutron stars and the composition of our galaxy. This thesis aims to propose a search method for these elusive signals and estimate its effectiveness and range on both current and next generation gravitational wave detectors.

Radboud Universiteit Nijmegen

Contents

Chapter 1

Introduction

This chapter intends to be a brief summary on the nature of gravitational waves (GWs) from isolated rotating rigid bodies on which this thesis is focused on. In the first half of this chapter, we give a brief overview on the motivations and efforts related to detecting periodic GWs. We also introduce the basic concepts that are essential to understanding the basic physics of GW astronomy. In the latter half of this chapter we state some of the assumptions on the nature of the GW detector and the effects that one must correct for in order to achieve successful detection.

1.1 Background and Motivation

The first successful detection of a GW event, GW150914, occurred on September 14th 2015 by the LIGO and virgo collaborations [1]. This signal, similar to the numerous detections since then, are the result of binary systems consisting of either a pair of neutron stars (NSs), a pair of black holes or both. Continuous GWs, resulting from an isolated non axis-symmetric rotating NS have not been detected as of the time of writing despite great efforts to do so by research groups such as the Max Planck Institute for Gravitational Wave Physics, the LSC-Virgo-KAGRA Continous Wave Group [2], [3] and by collaborative computing projects such as the Einstein@Home project [4].

The rewards for consistent and reliable detection of continuous GWs are two fold in the sense that they have the potential to shed light on two great mysteries:

1. What are the physical properties of NS interiors and how exactly are they structured?
2. Where are the missing fraction of NSs in our own galaxy?

The first mystery is rather self explanatory. The conditions under which the interiors of NSs are subjected to are too extreme to be studied in a laboratory. Furthermore, they are opaque to all forms of electromagnetic (EM) radiation making it impossible to directly observe their interiors. GWs on the other hand are highly sensitive to the structure of the body that is emitting them and therefore GWs can act as probe into the interior of NSs. The second mystery stems from the fact that while only approximately 2000 NSs have been observed in our galaxy, there is a predicted galactic population number on the order of at least hundreds of millions based off of the predicted number of supernova explosion events [5]. Currently, 236 pulsars have been cataloged and analyzed to determine whether they are a potential source for detectable GWs by the LIGO, virgo and KAGRA collaborations [6]. The overarching issue is that many NSs are emitting EM radiation at an intensity that is too low to be directly observed. GWs offer an alternative to observing these NSs and potentially any other non axially symmetric moving body that may be present in our galaxy.

There are a variety of search methods used to find periodic GWs from isolated rotating rigid bodies. The most basic and costly types of searches are called fully coherent searches, in which all available data is searched over coherently and matched against a signal waveform template. Meanwhile, more efficient "semi-coherent" search methods have been proposed such as the PowerFlux, Hough and Stackslide methods (see

chapter 3 for a discussion and overview). The search for ever more effective search methods and more efficient algorithms is an open and active area of research, with more sophisticated algorithms being continuously developed and implemented only recently [7].

This thesis is a search proposal for continuous GW signals that may last up to a few days, from newly born magnetars (NBMs) leftover from supernovae explosions. Our proposal is to use an adapted form of the semi-coherent Stackslide method, which again we describe in detail in chapter 3, to search for these elusive signals.

This thesis is outlined in the following way: In this introductory chapter we outline the basics of the nature of GWs, the GW detector and the technical corrections that must be performed in order to ensure successful detection; in chapter 2 we outline the specifics of GWs produced by NBMs as well as the conventional statistical tests that one must apply to claim a detection; in chapter 3 we introduce our search method, explain its necessity and quantify its sensitivity; in chapter 4 we give an overview on the general astrophysical properties of NSs and how they may effect the waveform signal; in chapter 5 we demonstrate the performance of our search method using realistic model parameters on a variety of GW detectors that are both currently active and future planned next generation detectors and finally in chapter 6 we discuss the implications of the limitations of our search, suggested parameter space ranges to search over and suggested improvements for both our search method and our NS models.

1.2 The Nature of Gravitational Waves

1.2.1 Basic Concepts

GWs are "ripples" in spacetime caused by accelerated masses, contingent on the motion not being completely axis-symmetric. The wave equations themselves emerge naturally from Einstein's theory of General Relativity by adding a small perturbation term to the Minkowski metric:

$$g_{\mu\nu} = \eta_{\mu\nu} + h_{\mu\nu}, \qquad |h_{\mu\nu}| << 1 \tag{1.1}$$

The Einstein equations can be derived using the metric [1.1] and subsequently written in a compact way using the harmonic gauge choice. We are interested in keeping terms that are only linear order in h. The resulting Einstein equations in this weak linearized gravity are:

$$\Box \bar{h}_{\mu\nu} = -\frac{16\pi G}{c^4} T_{\mu\nu} \tag{1.2}$$

Where we use the shorthand notation:

$$\bar{h}_{\mu\nu} = h_{\mu\nu} - \frac{1}{2}\eta_{\mu\nu}\eta^{\alpha\beta}h_{\alpha\beta} \tag{1.3}$$

The solution to [1.2] is a standard calculation and can be found using Green's functions and again written in a neat form using an appropriate gauge choice. Additionally, it is assumed that we are in the far-field approximation and that the source is non-relativistic in nature. The result in the so called transverse-traceless gauge is:

$$\bar{h}_{ij}(t,x) = \frac{2G}{c^4}\frac{d^2}{dt^2}Q_{ij}\left(t - \frac{r}{c}\right) \tag{1.4}$$

Where Q_{ij} is the quadrupole moment tensor and is defined as:

$$Q^{ij} = \int d^3x \rho(t,x)\left(x^i x^j - \frac{1}{3}r^2\delta^{ij}\right) \tag{1.5}$$

And the transverse-traceless gauge is a valid gauge choice in which we may write the metric perturbation in the following way for a GW travelling in the z-direction:

$$h_{ij}^{TT} = \begin{pmatrix} h_+ & h_\times & 0 \\ h_\times & -h_+ & 0 \\ 0 & 0 & 0 \end{pmatrix} \tag{1.6}$$

We may also write this in an equivalent form in terms of polarization tensors:

$$h_{ij}^{TT} = h_+ e_+ + h_\times e_\times \tag{1.7}$$

Equation [1.4] is the famous quadrupole formula which shows that GWs are produced by masses that move in such a way that their quadrupole moment tensor varies in time. Moreover, an analogy with EM radiation has been suggested by some authors [8] as an intuition to the meaning behind this formula. The reasoning is that as accelerated charged particles produce EM radiation related to their time varying dipole moment, accelerated masses produce GW radiation related to their time varying quadrupole moment. Since mass-energy is conserved, massive particles produce radiation related to their time varying quadrupole rather than their dipole moment. The quadrupolar nature of GWs also explains why GW detectors are often 2 dimensional whereas EM detectors are often constructed as one dimensional antennae.

1.2.2 Gravitational Waves from Non-Precessing Rotating Rigid Bodies

As this thesis will be focused on isolated rotating magnetars, it is useful to state some basic results from the GWs produced by a rotating rigid body to understand some of their basic properties before conducting a more in depth analysis. For simplicity we will assume that the magnetar that we are analyzing is ellipsoidally deformed. The following derivation for the h_+ and $h_\times$ strain components from rotating rigid bodies can be found in the literature [9]. The main results and ideas are summarized below.

The first step is to take the inertia tensor defined by:

$$I^{ij} = \int d^3x \rho(x)(r^2\delta^{ij} - x^i x^j) \tag{1.8}$$

in a diagonalized form $I^{ij} = diag(I_1, I_2, I_3)$, where I_1, I_2, I_3 are the principal moments of inertia of the ellipsoid. We can then calculate its form in a rotating frame using the standard tensor transformation law:

$$I'_{ij} = (\mathfrak{R} I \mathfrak{R}^T)_{ij} \tag{1.9}$$

where $\mathfrak{R}$ is a rotation matrix.

After carrying out this calculation explicitly and relating the inertia tensor to the quadrupole moment tensor in equation [1.4] the following result is obtained:

$$h_+ = \frac{G}{c^4 r} 4\omega^2 (I_1 - I_2) \frac{1 + \cos^2 i}{2} \cos(2\omega t) \tag{1.10}$$

$$h_\times = \frac{G}{c^4 r} 4\omega^2 (I_1 - I_2) \cos i \sin(2\omega t) \tag{1.11}$$

Where ω is the angular velocity of the body.

By inspection we can already deduce certain properties of GWs. Firstly, GWs have frequencies that are equal to twice the bodies rotational frequency. Secondly we can see that if $I_1 = I_2$ we have no GW radiation and therefore bodies that are perfectly axis-symmetric do not emit GWs as previously claimed. Finally, the inclination angle i is the angle between the spin-axis (z-axis) of the ellipsoid and the observers line of sight.

Therefore, from the equations above, we can see that if the observers line of sight aligns with the ellipsoids spin-axis ($i = 0$), strong circularly polarized waves are observed and conversely if $i = 90^0$, weaker linearly polarized waves are observed while elliptically polarized waves are observed for any intermediate inclination angle value.

Equations [1.15] and [1.16] can be re-written in the following way:

$$h_+ = \frac{4\pi^2 G I_3 \epsilon}{rc^4} f_{GW}^2 \frac{1+\cos^2 i}{2} \cos\left(2\pi f_{GW} t\right) \tag{1.12}$$

$$h_{\mathrm{x}} = \frac{4\pi^2 G I_3 \epsilon}{rc^4} f_{GW}^2 \cos i \sin(2\pi f_{GW} t) \tag{1.13}$$

Where ϵ is called the ellipticity and is defined as:

$$\epsilon = \frac{I_1 - I_2}{I_3} \tag{1.14}$$

Finally, in more compact and familiar notation, these equations are often written in the following shorthand notation:

$$h_+ = A_+ \cos(\Phi(t)) \tag{1.15}$$

$$h_{\mathrm{x}} = A_{\mathrm{x}} \sin(\Phi(t)) \tag{1.16}$$

Where $\Phi(t)$ is the phase of the GW and $A_{+,\mathrm{x}}$ are defined as:

$$A_+ = \frac{4\pi^2 G I_3 \epsilon}{rc^4} \frac{1+\cos^2 i}{2} \tag{1.17}$$

$$A_{\mathrm{x}} = \frac{4\pi^2 G I_3 \epsilon}{rc^4} \cos i \tag{1.18}$$

The amplitude expressions above are often written as:

$$A_+ = h_0 \frac{(1+\cos^2 i)}{2} \tag{1.19}$$

$$A_{\mathrm{x}} = h_0 \cos i \tag{1.20}$$

Where h_0 is known as the intrinsic amplitude and is defined as:

$$h_0 = \frac{4\pi^2 G I_3 \epsilon}{rc^4} \tag{1.21}$$

The strain expressions above will serve as the foundation for our amplitude model. We will also only consider deformations that results in an ellipsoidal configuration even though the strain expressions are quite general. Our ellipticity and frequency models will be discussed in succeeding chapters when we consider the case when the rotating rigid body is a newly born magnetar.

We now turn to the case where the rotating body is precessing, meaning that the the spin-axis is no longer stationary. The waveform for a precessing body will be important later in our analysis of newly born magnetars that may change from a precessing to a non-precessing configuration.

1.2.3 The Precession Case

In the previous section we summarized the derivation of the strain components for a non-precessing body. This derivation was carried out by performing a single rotation transformation in the x-y plane to transform from our chosen reference frame to the body frame. The non-precessing case is more difficult since there is a loss of symmetry and rather than performing a single rotation matrix to the inertia tensor, we now must apply three separate rotations to transform from the reference frame to the body frame.

The amplitudes of the strain components for a precessing body can be written in terms of its so called "wobble" angle α.

The resulting amplitudes for a body rotating about its symmetry axis (z-axis) are [9]:

$$h_+ = \frac{G}{c^4}\frac{(I_3 - I_1)\Omega^2}{r}\sin(2\alpha)\sin i\cos i\cos(\Omega t) + 2\frac{G}{c^4}\frac{(I_3 - I_1)\Omega^2}{r}\sin^2\alpha(1+\cos^2 i)\cos(2\Omega t) \tag{1.22}$$

$$h_\times = \frac{G}{c^4}\frac{(I_3 - I_1)\Omega^2}{r}\sin(\Omega t) + 4\frac{G}{c^4}\frac{(I_3 - I_1)\Omega^2}{r}\sin^2\alpha\cos i\sin(2\Omega t) \tag{1.23}$$

The angle α, commonly known as the "wobble" angle, is one of the 3 Euler angles that is the angle between the stars angular momentum axis in our chosen reference frame to the same axis in the rotating (body) frame. It should also be noted that now there are waves that are emitted at both the bodies rotational frequency and twice the bodies rotational frequency in the x-y plane.

The implications of these strain equations will be reviewed further in chapter 4 when we discuss neutron star astrophysics.

1.3 Energy and Angular Momentum of Gravitational Waves

In this section we take a brief look at the energy and angular momentum carried by GWs which will become relevant later when calculating the time-scales under which magnetars may emit GWs.

1.3.1 Energy

The amount of energy carried by GWs is another standard calculation and can be found readily in the literature. The derivation is carried out by studying how GWs generate curvature. To do this we define a perturbation over a non-flat background metric and calculate the associated energy-momentum tensor from the Einstein equations. The standard formula for the power carried by GWs, to quadratic order in h can be expressed in terms of the quadrupole moment tensor as:

$$\mathcal{L}_{GW} = \frac{G}{5c^5}\langle \dddot{Q}_{ij}\dddot{Q}_{ij}\rangle \tag{1.24}$$

This formula can be used to quantify the amount of rotational energy that GWs carry from a rotating rigid body which is is essential to understanding the time-scales for which GWs are detectable. This is discussed in more detail in the succeeding chapters.

1.3.2 Angular Momentum

The angular momentum carried by GWs is a relatively involved derivation but can also be found readily in the literature and can be derived most naturally by viewing gravity as a field theory.

As in the energy case, the radiated angular momentum, to linear order in h can be expressed in terms of the mass quadrupole moment tensor as:

$$\left(\frac{dL^i}{dt}\right) = \frac{2G}{5c^5}\epsilon^{ikl}\langle \ddot{Q}_{ka}\ddot{Q}_{la}\rangle \tag{1.25}$$

This formula will become useful for the analysis of precessing NS evolution discussed in chapter 4 and is the final fundamental concept related to GWs from rotating rigid bodies that is needed in order to proceed in our analysis of newly born magnetars.

In the latter half of this chapter we will introduce the GW detector and the effects that one must apply to achieve successful detection of a GW signal.

1.4 Signal at the Detector

In this section we look at how the detector responds to a generic GW signal. Since the detector's orientation and relative position between itself and the source effects the signal wave form it is imperative to take these factors into account. Furthermore, the detector is subject to noise caused by numerous factors such as the seismic activity in the Earth, thermal noise and for interferometers even radiation pressure from the photons impinging on the interferometer's mirrors can be a source of noise. It is therefore also important to consider what assumptions we choose to make about the nature of this detector noise.

1.4.1 Gravitational Waves at the Detector

The strain tensor is expressed in terms of some polarization basis e_{ij} as shown in [1.7]. Mathematically this can be written as:

$$h_{ij}(t) = \sum_{A=+,\mathrm{x}} e_{ij}^{A} h_A(t) \tag{1.26}$$

The time series output data by the GW detector however is a series of real numbers. Symbolically the strain value measured by the detector can thus be written as:

$$h(t) = \sum_{A+,\mathrm{x}} D^{ij} e_{ij}^{A} h_A(t) \tag{1.27}$$

Where D^{ij} is known as the detector tensor.

This motivates the us to write the signal at the detector as:

$$h(t) = F_+ h_+(t) + F_{\mathrm{x}} h_{\mathrm{x}}(t) \tag{1.28}$$

Where $F_{+,-}$ are known as detector pattern functions. The pattern functions represent the fact that the detector frame and GW frame do not coincide. In order to convert the GW frame to the detector frame we must make three individual rotations (see figure [1.1]). Two of the three rotations depend on the direction of propagation of the GW defined by the angles θ and ϕ in spherical coordinates. The third rotation is more subtle and is defined by the so called polarization angle ψ which is the angle of rotation of the polarization basis relative to a given reference basis generated by the basis e_+ and e_{x}.

Therefore our detector pattern functions are in fact dependent on three angles which also have an implicit time dependence:

$$F_{+,\mathrm{x}} \rightarrow F_{+,\mathrm{x}}(\theta, \phi, \psi) \tag{1.29}$$

Furthermore, the pattern functions can be written with terms that depend only on the polarization angle and terms that depend only on the angles defining the direction of propagation. This is done by transforming the polarization tensors in the usual way with rotation matrices. The result is:

$$F_+(\theta, \phi, \psi) = a(\theta, \phi) \cos 2\psi + b(\theta, \psi) \sin 2\psi \tag{1.30}$$

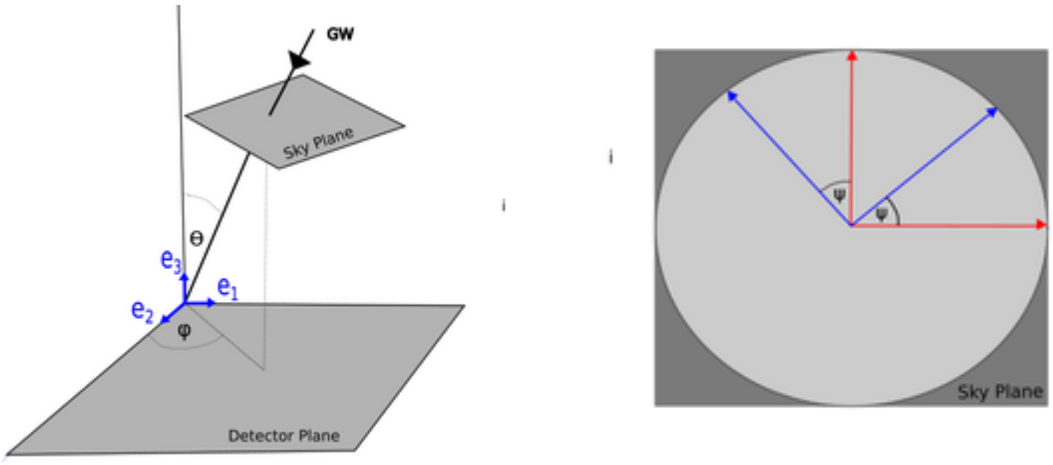

(a) Detector Geometry

(b) Sky Plane and Polarization Basis

Figure 1.1: The basic GW detector geometry. Figure (a) shows the direction of propagation of the GW and the detector frame defined by the blue basis vectors. Figure (b) shows the sky plane and the polarization angle between the red reference polarization basis and the waves blue polarization basis.

$$F_{\mathrm{x}}(\theta,\phi,\psi) = -a(\theta,\phi)\sin 2\psi + b(\theta,\psi)\cos 2\psi \tag{1.31}$$

Where a and b are functions of the detector position, orientation, the source sky location and angular velocity of the Earth.

With the expressions of the pattern functions above and using equations [1.15] and [1.16] we can finally write our GW signal [1.28] in its most canonical form; namely in terms of variables that depend only on the signals amplitude parameters and Doppler parameters. Ultimately then, our signal at the detector has the following form:

$$\begin{aligned} h(t) = {} & (a(\theta,\phi)\cos 2\psi + b(\theta,\psi)\sin 2\psi)A_{+}(\cos\Phi_0\cos\phi(t) - \sin\Phi_0\sin\phi(t)) \\ & +(-a(\theta,\phi)\sin 2\psi + b(\theta,\psi)\cos 2\psi)A_{\mathrm{x}}(\sin\Phi_0\cos\phi(t) + \cos\Phi_0\sin\phi(t)) \end{aligned} \tag{1.32}$$

Where the phase in equations [1.15] and [1.16] have been separated into an initial phase plus a time varying phase, $\Phi(t) = \Phi_0 + \phi(t)$.

The signal can be written in a much more elegant way that will be more convenient for future calculations:

$$h(t) = \sum_{i=1}^{4} A_i h_i \tag{1.33}$$

Where h and A have the following definitions:

$$h_1(t) = a(t)\cos\phi(t) \tag{1.34}$$

$$h_2(t) = b(t)\cos\phi(t) \tag{1.35}$$

$$h_3(t) = a(t)\sin\phi(t) \tag{1.36}$$
$$h_4(t) = b(t)\sin\phi(t) \tag{1.37}$$

$$A_1 = A_+\cos\Phi_0\cos 2\psi - A_\times\sin\Phi_0\sin 2\psi \tag{1.38}$$
$$A_2 = A_+\cos\Phi_0\sin 2\psi + A_\times\sin\Phi_0\cos 2\psi \tag{1.39}$$
$$A_3 = -A_+\sin\Phi_0\cos 2\psi - A_\times\cos\Phi_0\sin 2\psi \tag{1.40}$$
$$A_4 = -A_+\sin\Phi_0\sin 2\psi + A_\times\cos\Phi_0\cos 2\psi \tag{1.41}$$

1.4.2 Detector Noise

We assume the simple model that the signal that we would like to detect is a sum of the GW itself and noise:

$$x(t) = h(t) + n(t) \tag{1.42}$$

We also assume for simplicity that we are dealing with Gaussian noise with zero mean. In this case, the joint probability density function for observing multiple noise values is:

$$P(n_0, n_1, .., n_{N-1}) = \frac{exp[-\frac{1}{2}\sum_{i,j} C_{ij}^{-1} n_i n_j]}{\sqrt{(2\pi)^N \det C^{-1}}} \tag{1.43}$$

Which is just the usual probability density function (pdf) for a multivariate normal distribution with covariance matrix C_{ij}. A pdf, is simply a function whose value at any given sample gives the relative likelihood that the value of the random variable would be close to that sample value.

We can then use the following shorthand notation to write things in a more compact way as [10]:

$$(x|y) \equiv \sum_{ij} C_{ij}^{-1} x_i y_j \tag{1.44}$$

Using Parseval's theorem, the above shorthand notation can be shown to have the following form in the frequency domain:

$$(x|y) = 2\int_{-\infty}^{\infty} \frac{\tilde{x}^*(f)\tilde{y}(f)}{S_n(f)} df \tag{1.45}$$

Where $S_n(f)$ is the double sided noise spectral density and is usually defined in terms of the auto-correlation function $C(\tau) = \langle n(t+\tau)n(t)\rangle$ as:

$$S_n(f) = \int_{-\infty}^{\infty} C(\tau) e^{-2\pi f\tau} d\tau \tag{1.46}$$

Equation [1.45] then implies that:

$$(x|y) = 4Re\int_{0}^{\infty} \frac{\tilde{x}(f)\tilde{y}^*(f)}{S_n(f)} df \tag{1.47}$$

Similarly the pdf associated with observing a datum x(t) in the presence of a signal h(t) is given by:

$$\implies P(x|h) = \mathcal{N} e^{\frac{1}{2}((x-h)|(x-h))} \tag{1.48}$$

Where $\mathcal{N}$ is a normalisation constant.

1.5 Signal Modulation and Doppler Effect Introduction

In addition to the unique difficulties of detecting a GW signal from a newly born magnetar (see chapter 3), the signal modulation effects effecting all moving sources must also be considered to ensure successful detection. In general for any GW source of significant duration, there are a number of effects that can modulate both the frequency and amplitude of a GW signal. Looking at the signal received by the detector [1.33].

The two main effects are:

1. The Earth's rotation about its spin-axis and its orbit around the Sun changes the relative velocity between the detector and the source, resulting in a Doppler shift in the signals frequency.
2. The Earth's rotation changes the relative sky position of the source which changes the relative direction of propagation of the GW. Since the pattern functions depend on θ and ϕ [1.30, 1.31], the motion of the Earth induces an amplitude modulation.

Although a periodic GW source may emit monochromatic GWs at a single frequency, f_0, this will not be the frequency that is detected by a GW detector on Earth because of the Doppler effect due to the Earth's motion about its axis of rotation and its orbit around the Sun. In this section we summarize the basic equations for Doppler induced frequency modulation.

1.5.1 Basic Equations and Frequency Resolution

The observed frequency, f_{GW} received at the detector is given by the following formula to first order in $\frac{v}{c}$:

$$f_{GW} = f_{GW,0}\left(1 + \frac{\mathbf{v}\cdot\hat{\mathbf{r}}}{c}\right) \tag{1.49}$$

Where $\hat{\mathbf{r}}$ is a unit vector pointing from the observer to the source and $\mathbf{v}$ is the velocity of the observer relative to the source.

The main problem that arises is that $\mathbf{v}\cdot\hat{\mathbf{r}}$ is not constant. Thus we are interested in the change in frequency in a time T:

$$\begin{aligned}(\Delta f_{GW}) &= f_{GW} - f_{0,GW} \\ &= f_{0,GW}\left(\frac{\Delta v}{c}\right)\end{aligned} \tag{1.50}$$

Where Δv represents the change in velocity of the detector, in the direction of the source, in some time T_{obs}.

A crucial point is that the Doppler shift in frequency may be safely ignored if the change in the frequency due to this effect is smaller than our frequency resolution:

$$(\Delta f_{GW}) < \frac{1}{T_{obs}} \tag{1.51}$$

The inequality above is similar to our phase difference constraint given by [3.1]. We are interested in the maximum integration time T_{obs} for which the Doppler effect is negligible. We quantify this in the next subsection.

1.5.2 Earth's Rotation about its Axis

The linear velocity of the GW detector is simply given by:

$$v_{rot} = \omega_{rot} R_{\oplus} \cos(\theta_{lat}) \tag{1.52}$$

Where θ_{lat} is the angle of latitude on Earth. Additionally, the change in the angle due to the Earth's rotation, in some time interval T, given by:

$$\Delta\phi = \omega_{rot} T \tag{1.53}$$

If we assume that that the time interval T is sufficiently small, we can assume that the change in angle $\Delta\phi << 1$. Using the small angle approximation and some basic trigonometry we can say that the change in the component of velocity in the direction of the source is of order:

$$\begin{aligned} \frac{(\Delta v)_T}{v_{rot}} &\sim \Delta\phi \\ &\implies \Delta v \sim v_{rot}\omega_{rot} T \end{aligned} \tag{1.54}$$

Plugging this expression back into [1.51] we have the threshold condition:

$$\begin{aligned} & f_{0,GW}\left(\frac{(v_{rot})}{c}\right)\omega_{rot} T \sim \frac{1}{T} \\ \implies & T \sim \left(\frac{c}{f_{0,GW}\omega_{rot}^2 R_{\oplus}\cos\theta_{lat}}\right)^{\frac{1}{2}} \end{aligned} \tag{1.55}$$

A graphical representation of this formula can be seen in figure [1.2] below for the Advanced Virgo GW detector ($\theta_{lat} = 43.6^{\circ}$) and for an observer on the equator for a 1kHz wave.

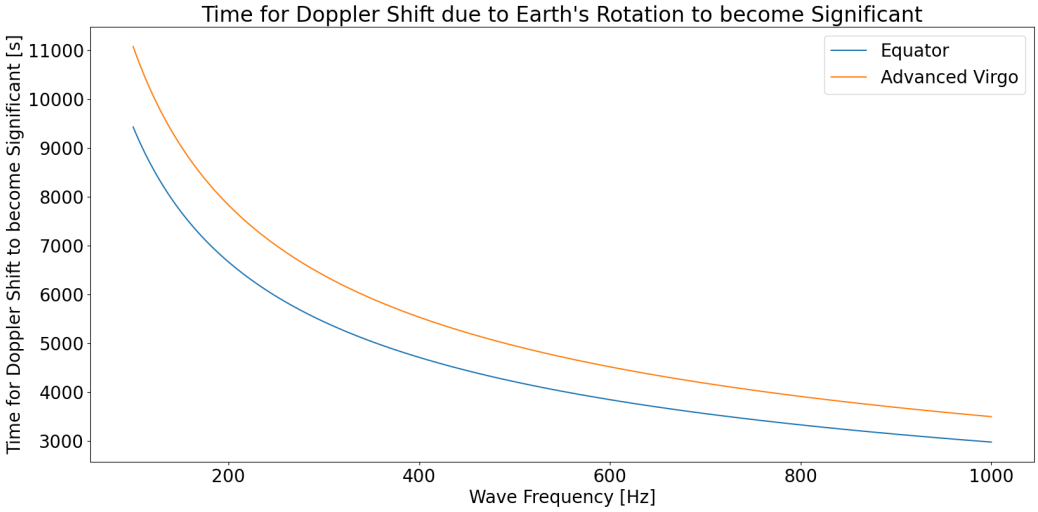

Figure 1.2: Times at which the Doppler effect due to the Earths rotation becomes significant for Advanced Virgo and an observer on the equator.

We can see that for a 1kHz wave, the Doppler effect due to the Earth's rotation becomes significant after approximately one hour.

We can also look at the maximum possible change in frequency due to the Earth's rotation. It is clear that this happens after 12h when the detectors velocity vector is completely reversed i.e. $\Delta v_{rot} = 2v_{rot}$

Using the above equations we can find that the maximum change in frequency is:

$$(\Delta f_{GW})^{max} = f_{0,GW} \frac{2\omega_{rot} R_{\oplus} \cos\theta_{lat}}{c} \tag{1.56}$$

Again just for completeness we can graph the maximum frequency change as a function of detector latitude seen in figure [1.3]

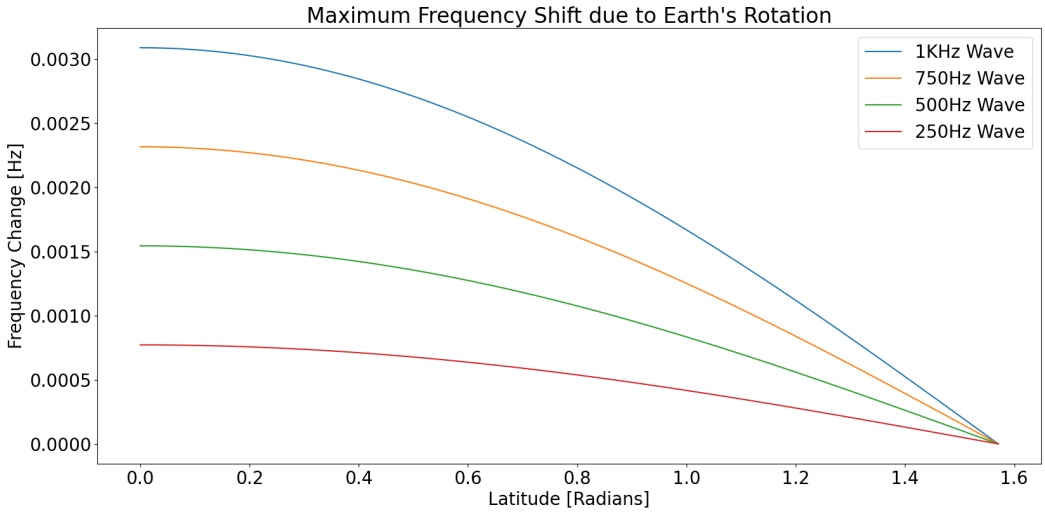

Figure 1.3: Maximum Doppler frequency shift due to Earth's Rotation as a function of latitude.

1.5.3 Earth's Orbit Around the Sun

Our analysis of the Earth's orbit around the Sun is identical to the previous subsection if we make the simplifying assumption that the Earth's orbit is circular with a radius of 1 astronomical unit. We will also take the orbital velocity to have a value of approximately $v_{orb} \approx 3 \times 10^4 m/s$

Using these values and [1.55] we can represent the threshold integration time such that the Doppler shift due to the Earth's orbit around the Sun is sufficiently small so that the frequency resolution condition is satisfied. As before, we show this graphically below in figure [1.4].

If we assume a GW with $f_{GW,0} = 1kHz$ we can conclude that the Doppler effect due to the Earth's Rotation becomes more important before the Doppler effect due to the Earth's orbit around the Sun. For the Earth's orbit around the Sun, the Doppler shift becomes significant after approximately 2 hours as opposed to 1 hour for the Earth's rotation.

As in the case of Earth's rotation we can similarly calculate the maximum frequency change due to Earth's orbit around the Sun, shown graphically in figure 1.5

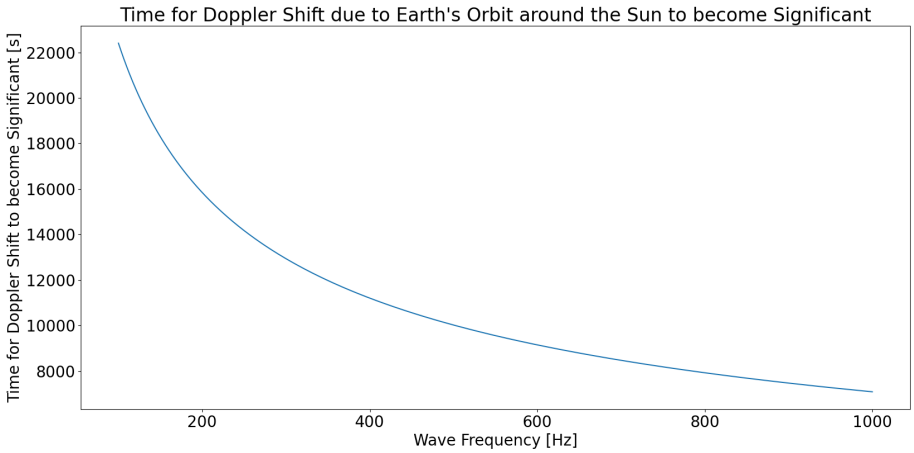

Figure 1.4: The time for which the Doppler effect due to the Earth's orbit around the Sun becomes significant

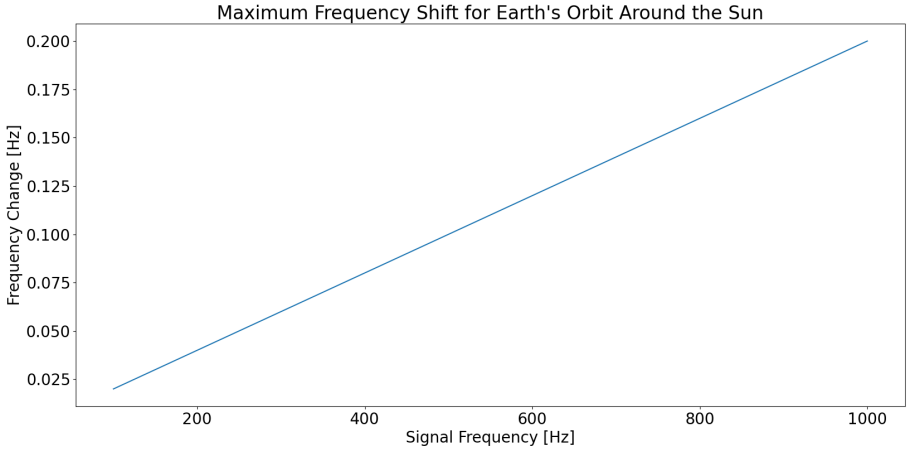

Figure 1.5: Maximum Doppler frequency change due to Earth's orbit around the Sun as a function of the wave frequency

1.5.4 Adjusting for the Doppler Effect

An obvious way one could imagine to deal with the Doppler effect due to the Earth's rotation and its orbit around the Sun is to redefine a new time coordinate:

$$t = t^{'} + \frac{y(t)}{c} \tag{1.57}$$

Or for a generic source location:

$$t = t^{'} + \frac{x(t) \cdot \hat{\mathbf{r}}}{c} \tag{1.58}$$

Where x(t) is the location of the detector with respect to the solar system barycenter for instance and $\hat{\mathbf{r}}$ is the unit vector pointing from the detector to the source. It is therefore imperative to adjust for the Doppler shift by re-defining our time variable according to:

$$t = t^{'} + \frac{x_{SSB}(t) \cdot \hat{\mathbf{r}}}{c} \tag{1.59}$$

Where $x_{SSB}(t)$ is the location of the detector with respect to the solar system barycenter and $\hat{\mathbf{r}}$ is the unit vector pointing from the detector to the source.

In general, GWs from NBMs are expected to be detectable over a period of days, depending on the spindown rate, and so the Doppler shift due to the Earth's rotation around the sun and the Doppler shift due to the Earths rotation about its axis both become important on these time scales.

1.6 Shapiro and Einstein Time Delay

There are a number of other caveats that must be taken into account to obtain the correct time shift in the GW arrival time. In the previous section the Doppler correction due to the Earths motion was discussed. The correction for the time coordinate was given by [1.59] when the solar system barycenter is used as a reference frame. This time delay is often referred to as Roemer Time Delay.

In addition, the general relativistic effects due to our solar system, effecting the propagation of waves, must also be taken into account. This time delay effect is known as Shapiro time delay. The Einstein time delay is a further correction that describes the shift in proper time rather than coordinate time [11]

Therefore, in practice the equation [1.59] can be more accurately written as:

$$t = t^{'} + \frac{x(t) \cdot \hat{\mathbf{r}}}{c} + \Delta_S - \Delta_E \tag{1.60}$$

Where the time delay effects due to the Shapiro and Einstein effects have been added.

Finally, for completeness, there may be other astrophysical effects that alter the time of arrival of GWs. One notable effect is that the interstellar medium may have a slightly altered refractive index due to the presence of ionized particles.

This concludes all of the basic phenomenon that must be understood in order to begin performing data analysis techniques on GW detector data, in order to perform a search which will be described in detail in the next chapter.

Chapter 2

Detecting Gravitational Waves from Newly Born Magnetars

In this chapter we give an outline of the problem at hand, namely trying to identify whether or not a GW signal is present in a (generally much larger) noise background. Generally, a detector will simply measure a time series of random variables with a certain distribution characterized by its probability density function. The basic problem in GW detection is to identify a gravitational waveform in a noisy background by assigning probabilities and appropriate statistical tests. We explain the method in which this is usually carried out, the F-Statistic approach, in the first half of this chapter. In the latter half of this chapter we explain our signal model for GWs produced by NBMs.

2.1 Maximum Likelihood and Hypothesis Testing

To begin this chapter we give an outline of the problem at hand, namely trying to determine whether or not a gravitational waveform is present in a noise background. The basic approach to GW detection is to quantify the probability of a gravitational waveform being present in a noisy background by assigning probabilities. Generally, a detector will simply measure a time series of random variables with a certain distribution characterized by its probability density function.

The goal is to determine whether the set of random variables produced by a detector has a pure noise pdf or a noise with signal pdf. An important property of Gaussian noise is that the noise power follows a χ^2 distribution with two degrees of freedom. It then follows that a GW signal in the presence of noise follows a non-central χ^2 distribution with 2 degrees of freedom.(see figure [2.1]).

There are many statistical tests one can perform to determine whether there is a GW present in the noise background or not. One of the most popular tests is called the Neyman-Pearson test, a popular Frequentist approach.(For a comparison between both Frequentist and Bayesian statistical tests in the context of targeted searches, please see [12]).

Looking at our signal model [1.42], we define the null hypothesis $\mathcal{H}_N$ as the assertion that there is only noise and no GW signal present and the hypothesis $\mathcal{H}_S$ as the assertion that a GW signal is present with noise. Symbolically these hypotheses can be written as:

$$\mathcal{H}_N : x(t) = n(t) \tag{2.1}$$

$$\mathcal{H}_S : x(t) = n(t) + h(t) \tag{2.2}$$

A detection statistic $\mathcal{D}$ is a real valued function that depends on the data and is chosen such that a particular value of this function $\mathcal{D}^*$ determines a threshold that a statistical test can decide between two hypotheses.

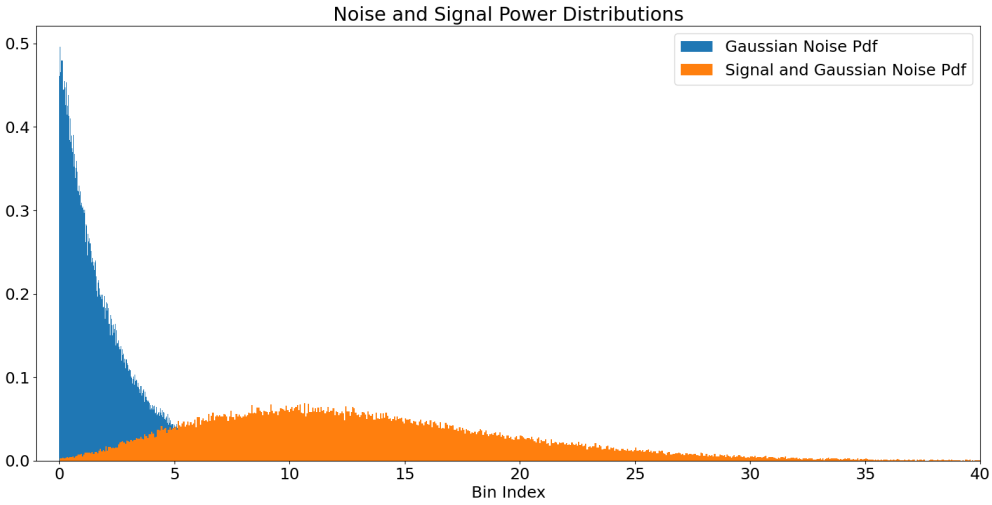

Figure 2.1: Gaussian noise and Gaussian noise with a signal present power distributions generated with Python3 using the Numpy librarys fast Fourier transform method. Gaussian Noise with zero mean follows a χ^2 distribution without a signal present and a non-central χ^2 distribution with a signal present.

A statistical test that decides between two hypotheses is subject to two errors known as the false alarm, defined by:

$$\alpha := \int_{\mathcal{D}*}^{\infty} P(\mathcal{D}|0)d\mathcal{D} \tag{2.3}$$

and the false dismissal:

$$\beta := \int_{-\infty}^{\mathcal{D}^*} P(\mathcal{D}|h)d\mathcal{D} \tag{2.4}$$

The false alarm is the defined as the probability that the noise power exceeds a given threshold resulting in a false detection and the false dismissal is defined as the probability that the signal power falls below this given threshold.

Ultimately the goal is to minimize the false dismissal probability for a given false alarm probability. The Neyman-Pearson lemma states that the most powerful method to achieve this is to maximize the so called likelihood ratio:

$$\Lambda = \frac{P(x|h)}{P(x|0)} \tag{2.5}$$

Where the numerator is the probability of observing the data given that the GW signal is present and the denominator is the the probability of observing the data given that the GW signal is absent.

Notice that the probability of observing the signal given that the GW is present, is equivalent to the probability of observing the data without the GW, given noise. In other words:

$$\Lambda = \frac{P(x-h|0)}{P(x|0)} \tag{2.6}$$

Substituting our Gaussian pdfs gives:

$$\Lambda = \frac{exp(-\frac{1}{2}(x-h|x-h))}{exp(-\frac{1}{2}(x|x)} \tag{2.7}$$

Cleaning up the expression and taking the logarithim yields:

$$\log \Lambda = (x|h) - \frac{1}{2}(h|h) \tag{2.8}$$

Notice that one of the advantages of writing the GW signal in the form [1.33] is that the calculation for the likelihood ratio becomes easier. Substituting our canonical form for h yields:

$$\log \Lambda = A_i(x|h_i) - \frac{1}{2}A^i A^j(h_i|h_j) \tag{2.9}$$

It is now simple to calculate the maximum likelihood estimator (MLE) of the amplitude parameters by finding the maximum of the above expression with respect to these amplitude parameters. The MLE turns out to be:

$$\hat{A}^j = (M^{-1})^{ij} X_i \tag{2.10}$$

Where:

$$M_{ij} \equiv (h_i|h_j) \tag{2.11}$$

$$X_i \equiv (x|h_i) \tag{2.12}$$

The so called F-Statistic is a detection statistic defined as the maximum of the log likelihood function over the amplitude parameters:

$$F = \log \Lambda\big|_{A=\hat{A}} \tag{2.13}$$

Finally:

$$F = \frac{1}{2}X_i(M^{-1})^{ij}X_j \tag{2.14}$$

The F-Statistic follows a χ^2 distribution with 4 degrees of freedom for each when a GW signal is absent and a non-central chi-squared distribution with 4 degrees of freedom when the GW signal is present. The 4 degrees of freedom correspond to each of the 4 unknown Doppler parameters.

The ensemble average of the twice the F statistic is given by:

$$\langle 2F \rangle = 4 + (h|h) \tag{2.15}$$

The distribution properties of the F-Statistic was shown by calculating the F-Statistic multiple times using the ComputeFstatistic_v2.c file from the LALApps library [13]. We performed each F-Statistic calculation for a signal with frequency between 99 and 101Hz over a small frequency bandwidth of $2 \times 10^{-4} Hz$ centered at 100.499 Hz. The signal data over which the F-Statistic was calculated was generated using the makefakedata_v5.c file from the same library. The LALApps software also takes into account the Doppler induced modulation effects described in chapter 1 by keeping track of the coordinates of the Sun and Earth. The result is shown in figure 2.2

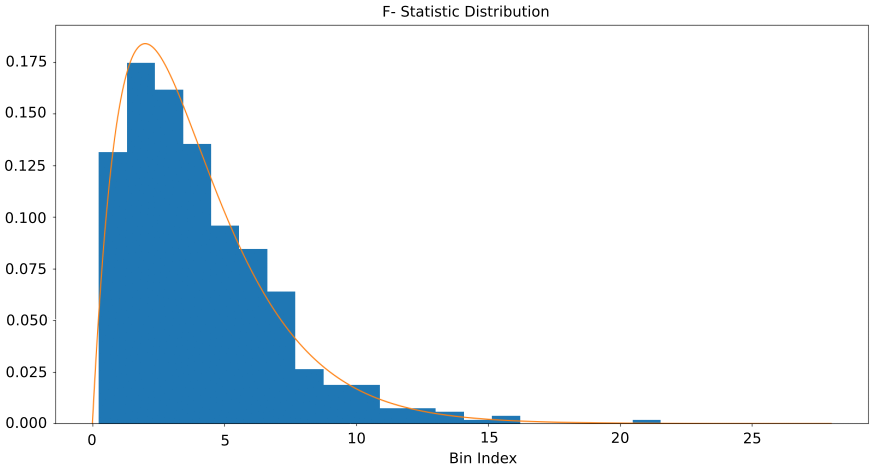

Figure 2.2: The F-Statistic distribution simulated with the makefakedata_v5.c file from the LALApps library. The F-statistic follows a χ^2 distribution with 4 degrees of freedom in the presence of noise only. The 4 degrees of freedom correspond to the 4 unknown Doppler parameters.

2.2 Frequency Model and Spindown

The two most important defining features of NBMs that are most relevant to consider when designing a search strategy for the GWs that they produce are apparent from its name:

- **Newly Born** - eluding to the fact that these sources are characterized by high rotational frequency and rapid spindown rates. Young NSs spin rapidly due to the conservation of angular momentum before and after the supernova explosion. As we will see in the next subsection, rapidly evolving frequency models can be problematic and computationally expensive to search for if the observation time is long.
- **Magnetar** - eluding to the fact that these sources have very high magnetic fields of values up to about $10^{15}G$. These strong magnetic fields deform the magnetar, altering its ellipticity and hence its GW amplitude. Understanding the extent to which these magnetic fields can deform the body is essential for modelling the amplitude and performing the search.

Phase/Frequency Model

The following frequency model that we adopt for our model has previously been used by Oliver et al. [14] to search for long duration GW transients using a weighted Hough transform search method and is quite general. A quick overview of this frequency model, that we also decide to adopt in this thesis, is given below.

In general, a neutron star will alter its rotational energy through a variety of processes such as EM torque and GW emission (spin-down) and accretion of nearby matter (spin-up). This can be summarised in the simple equation:

$$\dot{\Omega} = -\kappa\Omega^n \tag{2.16}$$

Where Ω is the angular frequency. Equation [2.16] is entirely general. The parameters n and κ are taken to be free parameters and can be chosen to best model any of the spindown causing phenomenon described above. The parameter n is known as the braking index and can in principle be measured by observing NS frequencies and their corresponding derivatives. It can be solved for by differentiating [2.16]:

$$n = \frac{\ddot{\Omega}\Omega}{\dot{\Omega}^2} \tag{2.17}$$

The value of the braking index corresponds to different spindown mechanisms. Notably, a braking index of n= 5 corresponds to the scenario where GWs are the dominant source of NS spindown [15]

The parameter κ can be related to the lifetime of the source by integrating [2.16] from the birth of the magnetar (t=0) to the sources lifetime τ. The result is:

$$\kappa = \frac{1}{\tau(n-1)}\left[\frac{1}{\Omega^{n-1}} - \frac{1}{\Omega_0^{n-1}}\right] \tag{2.18}$$

Also assuming that τ is sufficiently large such that $\Omega << \Omega_0$ gives:

$$\kappa = \frac{1}{\tau(n-1)}\left[\frac{1}{\Omega^{n-1}}\right] \tag{2.19}$$

Our frequency model then, is simply the general solution to [2.16] which is:

$$\boxed{f_{GW}(t) = f_{GW,0}\left(\frac{t-T_0}{\tau}+1\right)^{\frac{1}{1-n}}} \tag{2.20}$$

Where T_0 is the time at the birth of the magnetar. As we will see in the next chapter, this frequency model is especially difficult to work with due to how rapidly the frequency changes for a high braking index. In the next chapter we explain why the Frequentist F-Statistic approach outlined above is computationally unfeasible for frequency models such as this. This will serve as the primary motivation behind our search proposal.

Chapter 3

The Search

In this chapter we introduce our search method and explain its necessity due to the incompatibility between the common Frequentist based F-Statistic approach to detecting GWs and our frequency model properties. We describe in detail our search method and its relationship to the semi-coherent "Stackslide" search method. We then end this chapter by giving an expression for our search's sensitivity.

3.1 Motivation and Computational Expense

While our frequency model [2.20] originates from a straightforward derivation, it is a difficult model to work with especially in the case of a high braking index. As we saw in the previous chapter, one of the most common statistical tests to determine whether a signal is present in a noise background is using the Frequentist approach of maximizing the likelihood function and calculating the corresponding F-Statistic [2.14]. The calculation of the F-Statistic can be computationally expensive however since it is a matched filtering technique that essentially matches an observed signal to a signal template bank defined by a multi-dimensional parameter space. The number of templates needed and thus the dimensionality of the parameter space, scales non-linearly with the observation time (see below). Therefore, the F-Statistic is usually calculated either for systems with a rapidly varying frequency (requiring spindown parameters and corresponding higher dimensional parameter space) over a very short observation time or for a system with a slowly varying frequency (lower dimensional parameter space) over a long observation time. An example of the former is a binary merger which is a system with a rapidly changing frequency over a very small observation time, a so called GW transient signal while an example of the latter is an old deformed NS that is producing near monochromatic GW signals.

This F-Statistic approach is uniquely difficult in the case of NBMs precisely because it is a system with a rapidly changing frequency [2.20] observed over a relatively long observation time. Therefore, a large number of spindown parameters are needed to carry out the calculation. To see this explicitly, consider the following condition that must be met to ensure sufficient frequency resolution for a Taylor expanded approximation of our frequency model:

$$\left| f_{GW}(t) - \sum_{n=0}^{N} \frac{f_{GW}^{(n)}}{n!}(t)^n \right| < \frac{1}{T_{obs}} \tag{3.1}$$

The above inequality ensures that the phase difference between the templates and our frequency model do not differ by more than one cycle over the entire observation time. The term on the far left is our frequency model [2.20] that is a function of time. This term reflects how we expect the frequency evolution to occur. The next term is our Taylor expansion approximation expanded around the time variable t which expresses our frequency model written as a sum of spindown parameters.

Substituting our model for $n = 5$, $\tau = 10000s$ and $f_{GW,0} = 1000Hz$ and assuming we only observe the signal for 5000 seconds gives:

$$\left|1000\left(\frac{t}{10000}+1\right)^{-\frac{1}{4}} - \left[1000 - \frac{t}{40} + \frac{t^2}{640000} + higherorder\right]\right| < 2\times 10^{-4} \tag{3.2}$$

We performed this calculation and it was found that unfortunately, for the inequality to hold from time $t = 0$ to $t = T_{obs}$, we need 16 terms in the Taylor expansion approximation for reasonable values of τ and breaking index n for our frequency model. This effectively rules out the F-statistic approach in our case, and motivates an alternative statistical test and a corresponding alternative detection statistic choice in order to search for these uniquely elusive type of continuous GW signals.

The main approach that we considered to take to resolve this issue is to adopt a modified semi-coherent search method that is uniquely adapted to dealing with our frequency model.

For this approach, the approach that we ultimately decided to adopt in this thesis, is to modify some existing semi-coherent search method that will avoid the computational expense constraints that our frequency model is subject to. This method, our search proposal, will now be fully expanded upon and explained below.

3.2 Semi-coherent Searches and StackSlide Introduction

We now wish to propose a search method that will avoid dealing with a computationally expensive and large parameter space. Generally speaking there are two categories of search methods used in GW astronomy. The most sensitive and computationally intensive types of searches are fully coherent, in which all available data is combined coherently and matched against the signal waveform. The smallest detectable signal amplitude for fully coherent searches falls as $\sqrt{N}$, where N is the quantity of data. Therefore, the search becomes more sensitive as more data is collected. The issue is that the large observation times become computationally expensive for coherent searches. The reason for this is that the number of templates needed for matched filtering to conduct a fully coherent search scales with some higher power of the observation time, at least T_{obs}^5 for only a single spindown parameter [16]. Furthermore, these fully coherent searches become more computationally expensive for younger, faster spinning, higher spindown neutron stars, that require more spindown parameters and a corresponding higher dimensional parameter space. In contrast, older slowly spinning neutron stars are less computationally expensive for the same reasons. For an overview on the detailed calculations see [17]. In short, the best sensitivity, gained with fully coherent searches, is gained at very high computational expense.

Semi-coherent searches, in essence, exchange sensitivity for less computational expense. Semi-coherent searches are implemented by first dividing the data into N segments, then each segment is Fourier transformed and searched coherently over. Finally the segments are then recombined incoherently by some chosen method. Semi-coherent searches are much more computationally feasible because the time of each segment may be relatively small and the number of templates needed to search over varies non-linearly with the time as previously discussed. In short, semi-coherent searches are faster because of the shorter time base-line of each segment but at the cost of losing phase information between each segment.

Dividing the signal into segments is useful in our case as the signal we are searching for has a frequency that varies so rapidly and we wish to be able to analyze a certain fraction of a frequency bin at any one time. How to choose the length of each segment is an important question when dealing with signals of rapidly changing frequency and will be discussed in detail in the next section.

Next, assuming that the length of each segment has been chosen, there is still the question of how to recombine each of these segments as the next step in the search proposal. Some of the most common semi-coherent search methods are the "StackSlide", "Weighted Hough" and "Powerflux" methods. (See [18] for an overview). In this thesis we propose a modified version of the Stackslide method with the important difference being that we will impose our own criterion on choosing the segment lengths. In the StackSlide method, one performs a so called short-time Fourier transform (SFT) in each segment and then one "slides"

the frequency bins of each Fourier transformed segment to line-up the signal peaks and then the power from each segment is simply summed ("stacked").

3.3 The Short-Time Fourier Transform

Typically in GW searches for monochromatic signals, an SFT length of $T_{SFT} = 1800s$ is used to ensure sufficient resolution without any Doppler or other time delay effects becoming significant. Our search method is a modified version of the Stackslide search in the sense that we will use SFT lengths of different duration. This is because in our search, the frequency model dictates that the signals frequency changes rapidly in time, particularly early on. Therefore, when analyzing the data in the frequency domain, it is useful to take a sequence of SFTs of different lengths. In our search proposal we choose SFT lengths such that each SFT contains no more than $\frac{1}{4}$ of a cycle of the phase (see [11]).

Namely, we want the following condition to hold:

$$\boxed{\dot{f}T_{SFT}^2 < \frac{1}{4}} \tag{3.3}$$

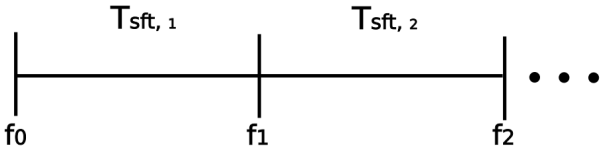

Figure 3.1: SFT Lengths

Where:

$$\dot{f} = \frac{f_2 - f_1}{T_{SFT}} \tag{3.4}$$

And so the inequality to solve is:

$$(f_2 - f_1)T_{SFT} < \frac{1}{4} \tag{3.5}$$

The above inequality can be solved iteratively using Python3 or any other appropriate software by substituting our frequency model [2.20].

With the above inequality we can calculate the number of SFT segments that are needed for a given total observation time as well as the required length of each individual SFT to satisfy the $\frac{1}{4}$ cycle criterion. Both of these calculation results are displayed, for 3000 SFTs, in figures [3.2, 3.3] below.

From figure [3.2] it can be seen that in order for the $\frac{1}{4}$ cycle criterion to be satisfied, the first SFT lengths are on the order of 10 seconds when the magnetar is rapidly spinning down. For later SFTs, as the magnetar is spinning down more slowly, the lenghts increase to approximately 250 seconds. It should also be emphasized that this is an entirely unconventional approach and choosing SFTs of different length in searches for continuous GWs has not yet been implemented or suggested in the current literature.

From figure [3.3], we see that for 3000 SFTs we already reach a total observation time of 500000 seconds. In this time, by our frequency model [2.20], a NBM with an initial rotational frequency of 1000Hz and emitting GW radiation only, will have spinned down to approximately 350Hz in this time.

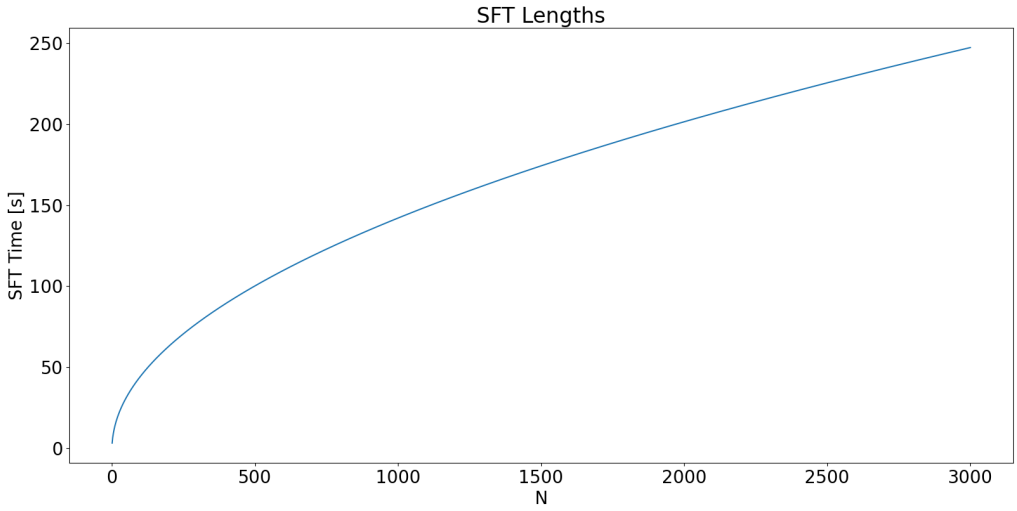

Figure 3.2: SFT Lengths for our frequency model with n=5 and $\tau = 10000$. As expected, earlier SFTs must be of shorter duration when the frequency is changing more rapidly and can be longer in duration for later SFTs when the frequency is evolving more slowly.

3.4 Detection Statistic and Non-Centrality Parameter

As discussed above, the Frequentist F-statistic approach is not a viable option for our frequency model. Therefore, we want to perform an alternative statistical test in each SFT to determine whether a signal is present. We do this by following the Stackslide method which uses not the F-statistic, but the signal power as the detection statistic. We then simply apply the same statistical analysis as explained in Chapter 2, namely calculating the false alarm and false dismissal probabilities by setting a threshold on the normalised power in the i^{th} SFT at frequency bin k, given by:

$$\rho_{i,k} = \frac{2|\tilde{x}_i[f_k]|^2}{T_{SFT}S_n[f_k]} \tag{3.6}$$

As mentioned, we assume that we are dealing with Gaussian noise with zero mean and therefore the normalised signal power in each SFT follows a non-central χ^2 distribution with 2 degrees of freedom and non-centrality parameter:

$$\lambda_i = \frac{4|\tilde{h}_i[f_k]|^2}{T_{SFT}S_n[f_k]} \tag{3.7}$$

Where again $S_n[f_k]$ is the noise power at a frequency bin k. Equation [3.7] shows that the more segments we sum together, the more likely we are to observe a GW signal provided the the noise power is sufficiently small. We may use this non-centrality parameter to calculate the range of our search. We show this calculation in detail in the next subsection.

3.5 Sensitivity

We now want to perform an estimate of the sensitivity of our modified Stackslide search method. In other words, the goal of this section is to answer the following question: "Given a false alarm probability, what is the smallest amplitude that will give at most a chosen false dismissal probability?" If the smallest detectable

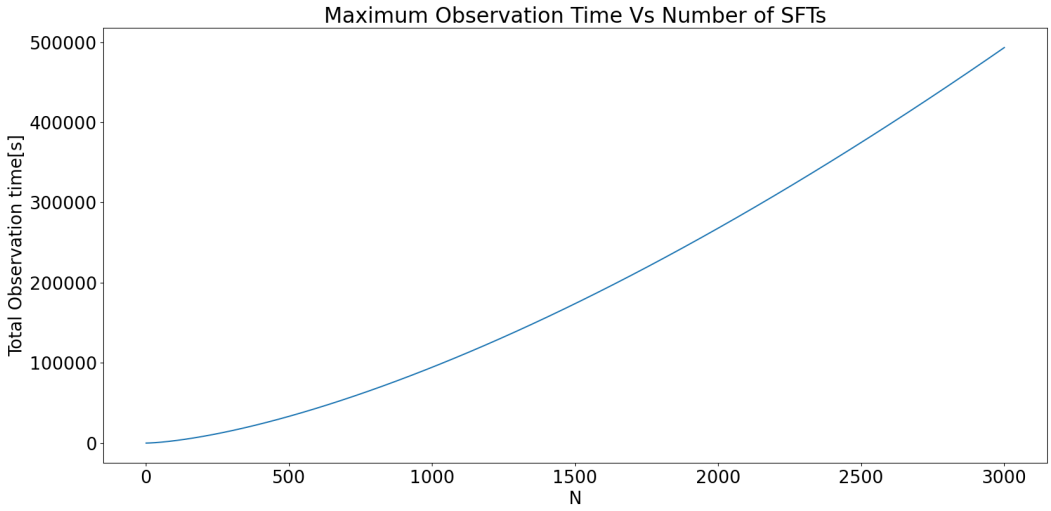

Figure 3.3: The maximum observation time for a given number of SFTs.

amplitude can be calculated then the corresponding maximum threshold distance between the source and the detector can also be calculated since the amplitude $h_0 \propto \frac{1}{r}$.

3.5.1 False Alarm

As described in Chapter 1 [2.3], the false alarm probability is defined as the probability of the noise power, without a signal present, being above a chosen threshold. It can be written as:

$$\int_{x_{th}}^{\infty} P(x|0)dx = \alpha \tag{3.8}$$

Now we can choose our false alarm probability to be any value that is desirable. In our case we choose it to be 1%. Notice that in the absence of a signal, the noise power follows a χ^2 distribution (see figure[2.1]) and so our equation becomes:

$$\int_{x_{th}}^{\infty} f(x;k)dx = 0.01 \tag{3.9}$$

Where $f(x;k)$ is the pdf for the χ^2 distribution with k degrees of freedom.

In our modified Stackslide search method we simply add the power from each SFT. Furthermore the sum of independent χ^2 random variables are themselves distributed as a χ^2 distribution with a degree of freedom equal to the sum of the individual degrees of freedom. Finally, as shown in chapter 1, each χ^2 noise random variable has 2 degrees of freedom in each SFT and so we get:

$$\int_{x_{th}}^{\infty} f(x, 2N_{sft})dx = 0.01 \tag{3.10}$$

Next, we can write the above expression in terms of the cumulative distribution function (cdf):

$$F(x_{th}; 2N_{sft}) = 0.99 \tag{3.11}$$

Where F(x) is the cdf of the χ^2 squared distribution. From here we can apply the inverse cdf function to both sides of the equation to get:

$$x_{th} = F^{-1}(0.99, 2N_{sft})) \tag{3.12}$$

We can solve this equation numerically to find x_{th} in terms of N. Using the SciPy python library we can solve this equation for a range of Ns and fit a linear curve to find the dependence of x_{th} on N.

To a good approximation and for sufficiently large N, we found this to be:

$$\boxed{x_{th} = 2.08N + 58.57} \tag{3.13}$$

3.5.2 False Dismissal

Now that we know our threshold, we can find the smallest amplitude, for a given false alarm probability, that will give a chosen false dismissal probability, in our case we choose this to be 10%.

When the signal is present, the power follows a non-central χ^2 distribution. As in the pure noise case, the sum of non-central χ^2 random variables are distributed as a non-central χ^2 distribution with additive degrees of freedom and additive non-centrality parameter. Our integral to solve is then given by:

$$\int_0^{x_{th}} f(x; 2N, \Lambda)dx = 0.10 \tag{3.14}$$

Where f in this case is the non-central χ^2 pdf with 2N degrees of freedom and a non centrality parameter Λ.

As before we can write this in terms of the cdf:

$$F(x_{th}; 2N, \Lambda) = 0.10 \tag{3.15}$$

Taking the inverse cdf of both sides gives:

$$x_{th} = F^{-1}(0.10, 2N, \Lambda) \tag{3.16}$$

Using the threshold found earlier in equation [3.13] we get:

$$2.08N + 58.57 = F^{-1}(0.10, 2N, \Lambda) \tag{3.17}$$

If we can find the non-centrality parameter Λ that satisfies the equation above, then we can find the minimum amplitude than can be detected for a given N. The non-centrality parameter is given by:

$$\Lambda = \sum_{i=1}^{N} \lambda_i \tag{3.18}$$

Where λ_i is the non-centrality parameter in each SFT. We can also average over inclination angle, polarization angle, declination and ascension angles and use the explicit definition of the non-centrality parameter 3.7 to get:

$$\langle \Lambda \rangle_{i,\alpha,\delta,\psi} = \sum_{i}^{N} \frac{7}{64} \frac{T_{SFT,i}}{S_n(f_i)} h_{0,i}^2 \tag{3.19}$$

We can then substitute our expression for the amplitude h_0 1.21:

$$\Lambda = \sum_{i}^{N} \frac{7}{64} \frac{T_{SFT,i}}{S_n(f_i)} \left(\frac{4\pi^2 G}{c^4} \frac{I_{zz}\epsilon}{r} f_{GW}^2(t_i) \right)^2 \tag{3.20}$$

Equation [3.20] is all we need to calculate the threshold range of our search proposal. To make this expression more explicit we can substitute our frequency model [2.20]:

$$\Lambda = \frac{7}{64} \frac{4\pi^2 G I_{zz}}{c^4 r} \sum_{i}^{N} \frac{T_{SFT}}{S_n(f_i)} \epsilon f_{GW,0}^4 \left(\left(\frac{t_i}{\tau} + 1 \right)^{\frac{1}{1-n}} \right)^4 \tag{3.21}$$

We can then make the distinction between two important cases, one when the ellipticity is constant, in which case the above expression simply becomes:

$$\Lambda = K^2 \sum_{i}^{N} \frac{T_{SFT}}{S_n(f_i)} \left(\left(\frac{t_i}{\tau} + 1 \right)^{\frac{1}{1-n}} \right)^4 \tag{3.22}$$

Where K is a constant.

It should be noted that in all likelihood the ellipticity is a time varying parameter that may change due to a number of astrophysical effects. In the case where the ellipticity changes significantly on the given time scales, it must also be incorporated into the sum above:

$$\Lambda = k^2 \sum_{i}^{N} \frac{T_{SFT}}{S_n(f_i)} \epsilon_i \left(\left(\frac{t_i}{\tau} + 1 \right)^{\frac{1}{1-n}} \right)^4 \tag{3.23}$$

The topic of magnetically induced ellipticity and the prospects of the ellipticity changing in time solely due to the magnetic field evolution, along with other physical caveats will be discussed in the next chapter.

Chapter 4

Neutron Star Astrophysics

In this chapter we explore the rich subject of neutron star astrophysics. While this thesis is in essence a search proposal, it is important to understand the nature of the signal sources. It is important not just to understand how the signal waveform is effected by the nature of the source but also to understand what GW signals and (hopefully reliable) future detections, will help us learn about the nature and structure of neutron stars themselves.

4.1 The Magnetic Field and Deformations

In this section we briefly characterize the newly born magnetars magnetic field and its effect on the ellipticity and therefore the deformation of the body itself.

4.1.1 The Magnetic Field

As notation we often write the magnetic field of the magnetar in terms of its poloidal and toroidal components:

$$B_p = (B_r, B_\theta, 0) \tag{4.1}$$

$$B_t = (0, 0, B_\phi) \tag{4.2}$$

In our case we will only consider stars with purely toroidal fields which are essential for GW emission (see below).

To begin we will make clear how we will model the NS that we wish to analyze. We will consider stars with a polytropic density profile with a superconducting fluid interior with the potential to form an outer crust given sufficient cooling. Specifically, we will assume that the star has an n=1 polytropic density profile. Finally, for the purposes of a rough estimate for the magnetically induced ellipticity, we will assume that the stars rotation has a negligible effect on the interior fluid dynamics.

We want to derive the form of the magnetohydrodynamic (MHD) equilibrium equations in order to understand the behaviour of the magnetic field. We will furthermore make use of the assumption that the fluid has no resistivity (infinite conductivity). The MHD equilibrium equations for this fluid then take a simplified form:

$$\frac{\nabla p}{\rho} = \frac{f_{Lorentz}}{\rho} + \rho \mathbf{g} \tag{4.3}$$

Where p is the pressure, ρ is the density and $\mathbf{g}$ is given by -$\nabla\Phi$ where Φ is the gravitational potential and obeys the Poisson equation:

$$\nabla^2\Phi = 4\pi G\rho \tag{4.4}$$

The Lorentz force for a continuous charge distribution can be written explicitly as:

$$f_{Lorentz} = \rho_c E + J \times B \tag{4.5}$$

In our case, we are dealing with a perfect conductor and thus the interior electric field must vanish giving:

$$f_{Lorentz} = \frac{(\nabla \times B) \times B}{4\pi} \tag{4.6}$$

Where the current density J was rewritten using the Ampère-Maxwell equation.

Substituting this back into [4.3] gives:

$$\frac{\nabla p}{\rho} + \nabla\Phi = \frac{(\nabla \times B) \times B}{4\pi\rho} \tag{4.7}$$

As stated, for this model we will assume that the NS has a barotropic equation of state:

$$\rho = \rho(p) \tag{4.8}$$

It should be noted that this is one of the most simple equation of states and in reality the density of the star depend on other parameters such as the temperature. Then, following Roxburgh [19], we can take the curl of [4.7] to get an equation for the magnetic field:

$$\nabla \times \left[\frac{B \times (\nabla \times B)}{\rho}\right] = 0 \tag{4.9}$$

Equation [4.9] completely determines the constraints on the magnetic field for our model. We can write the magnetic field in terms of Stoke's stream functions:

$$B_r = \frac{1}{r^2 \sin\theta}\frac{\partial\Psi}{\partial\theta} \tag{4.10}$$

$$B_\theta = -\frac{1}{r\sin\theta}\frac{\partial\Psi}{\partial r} \tag{4.11}$$

Finally using another result from Roxburgh:

$$B_p \cdot \nabla(r\sin\theta B_t) = 0 \tag{4.12}$$

which implies that we can express the toroidal component of the magnetic field as:

$$B_\phi = \frac{f(\Psi)}{r\sin\theta} \tag{4.13}$$

Where f is some function of the steam function Ψ.

This concludes the conditions that the magnetic field components must obey for this type of neutron star. Next we will explicitly state the exact form of our barotropic equation of state described in [4.8]

n=1 Polytope

For our analysis we will consider the so called n=1 polytrope model, which is considered to be quite accurate in describing realistic neutron stars, for our equation of state [4.8]. In this model the pressure of the star depends on its density according to:

$$P = K\rho^{1+\frac{1}{n}} \tag{4.14}$$

By solving Einstein's equations for a spherically symmetric, time-independent metric and imposing the non-relativistic limit we arrive at the Lane-Emden equation:

$$\frac{1}{\xi^2}\frac{d}{d\xi}\left(\xi^2\frac{d\theta}{d\xi}\right) + \theta^n = 0 \tag{4.15}$$

Where θ is related to the density and ξ is given by:

$$\rho = \rho_c\theta^n \tag{4.16}$$

$$\xi = r\left(\frac{1}{2\pi G}K\right)^{\frac{1}{2}} \tag{4.17}$$

and ρ_c is the central density.

A solution of the Lane-Emden equation for the case that n=1 is:

$$\theta(y) = \frac{\sin y}{y} \tag{4.18}$$

And therefore we consider a density profile of the form:

$$\rho(y) = \rho_c\frac{\sin y}{y} \tag{4.19}$$

Where y is defined as a dimensionless radius:

$$y = \frac{\pi r}{R} \tag{4.20}$$

4.1.2 Magnetic Deformations for Purely Toroidal Magnetic Fields

We are now ready to look to what extent a magnetic field distorts a neutron star in the case of purely toroidal magnetic fields. The following calculations have previously been performed by Zamani & Bigedli [20].

To begin, we assume that we can write the pressure, density and gravitational potential as a multipole expansion in terms of Legendre polynomials:

$$\rho(r,\theta) = \rho_0(r) + \delta\rho(r)P_l(\cos\theta) \tag{4.21}$$

$$p(r,\theta) = p_0(r) + \delta p(r)P_l(\cos\theta) \tag{4.22}$$

$$\Phi(r,\theta) = \Phi_0(r) + \delta\Phi(r)P_l(\cos\theta) \tag{4.23}$$

Furthermore, we will assume that the perturbed surface is described by the equation:

$$x(R,\theta) = R[1 + e(R)P_l(\cos\theta)] \tag{4.24}$$

We can then find the (r,θ) components of the perturbed versions of [4.7], keeping terms up to only first order in the perturbation:

$$\left(\frac{d\delta p}{dr} + \rho\frac{d\delta\Phi}{dr} + \delta\rho\frac{d\Phi}{dr}\right)P_l = \frac{[(\nabla\times B)\times B]_r}{4\pi} = \frac{f_r}{4\pi} \tag{4.25}$$

$$(\delta p + \rho\delta\Phi)\frac{dP_l}{d\theta} = r\frac{[(\nabla\times B)\times B]_\theta}{4\pi} = \frac{rf_\theta}{4\pi} \tag{4.26}$$

Along with the perturbed Poisson equation [4.4]:

$$\frac{d^2\delta\Phi}{dr^2} + \frac{2}{r}\frac{d\delta\Phi}{dr} - \frac{6}{r^2}\delta\Phi = 4\pi G\delta\rho \tag{4.27}$$

Next, we can find out how our magnetic field behaves by substitutions a purely toroidal field $B = (0,0,B_\phi)$ into [4.9]. The result is:

$$\frac{\partial}{\partial r}\left(\frac{B_\phi}{\rho r\sin\theta}\right)\frac{\partial}{\partial\theta}(B_\phi r\sin\theta) - \frac{\partial}{\partial\theta}\left(\frac{B_\phi}{\rho r\sin\theta}\right)\frac{\partial}{\partial r}(B_\phi r\sin\theta) = 0 \tag{4.28}$$

Substituting [4.19] into [4.28] and tidying up gives:

$$\left(\frac{\partial B_\phi}{\partial r} - B_\phi\cot y\frac{\pi}{R}\right)\left(r\sin\theta\frac{\partial B_\phi}{\partial\theta} + rB_\phi\cos\theta\right) - \left(\sin\theta\frac{\partial B_\phi}{\partial\theta} - B_\phi\cos\theta\right)\left(r\frac{\partial B_\phi}{\partial r} + B_\phi\right) = 0 \tag{4.29}$$

Which has the solution:

$$B_\phi = \frac{B}{\pi}\sin(y)\sin\theta \tag{4.30}$$

Where B is a constant. Following the calculations of Haskell et al. [21] we can find the form of the l=2 components of the Lorentz force by substituting [4.30] into [4.25] and [4.26]:

$$f_r = \frac{2B^2}{3\pi Ry}(\sin y + y\cos y)\sin yP_2(\theta) \tag{4.31}$$

$$f_\theta = \frac{2B^2}{3Ry}\sin^2 y\frac{dP_2}{d\theta} \tag{4.32}$$

The perturbed density can be solved for in terms of the gravitational potential using [4.25 and 4.26] above:

$$\delta\rho = -\frac{1}{24R^2\rho_c G\pi^2}(6\pi^3\rho_c\delta\Phi - B^2 y\sin y) \tag{4.33}$$

The perturbed gravitational potential can then be found using the perturbed Poisson equation [4.27]:

$$\delta\Phi = -\frac{B^2}{36\pi^3\rho_c y^3}[(5\pi^2(3-y^2)\sin y + (y^5 - 15\pi^2 y)\cos y] \tag{4.34}$$

Finally, the ellipticity is found in the usual way by using the definition [1.14]. The calculation is quite involved and is shown in detail in Appendix A.

The results of the calculation can be re-written in a more informative way as:

$$\epsilon \approx -1 \times 10^{-11} \left(\frac{R}{10km}\right)^4 \left(\frac{M}{1.4M_\odot}\right)^{-2} \left(\frac{\bar{B}}{10^{12}G}\right)^2 \tag{4.35}$$

Where we have used the approximation that the average field $\bar{B} \approx -0.17B$. Furthermore, by our calculations, we find that the ellipticity is about an order of magnitude larger than that provided by Haskell et al.

Finally, it is useful to take a moment to consider how these physical properties of the neutron star directly effect the amplitude of the GW since the amplitude h_0 is linearly proportional to ϵ.

4.2 Time Scales and Magnetar Evolution

One of the most important points to address is the matter of how long NSs with strong magnetic fields are expected to emit GWs. Clearly the stars finite rotational energy reservoir may be depleted primarily by EM torques thus hindering GW output. Strictly speaking the NS may also experience spin-up effects due to accretion of nearby matter however we will not consider this further.

In addition,in his 2002 paper, Cutler [22] showed that NSs with large toroidal magnetic fields deform into an unstable prolate configuration and subsequently tend to evolve into strong GW emitters. Therefore if we use this as our dynamical model then there is the additional issue of how fast would a NS, initially in an unstable prolate configuration (minimal GW emission), evolve to an oblate (maximal GW emission) configuration.

This process must evolve quickly enough since the NS may lose all of its finite rotational energy through EM radiation in its prolate configuration and have no energy left to fuel its GW emission by the time it ends up in its optimal GW prolate configuration. This issue is described in more detail in the next subsection.

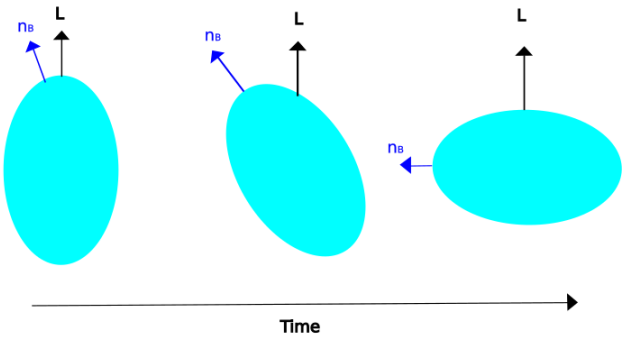

Figure 4.1: A sketch of the time evolution of a neutron star with a toroidal magnetic field. Initially the star is in a prolate shape where the magnetic axis n_B is almost aligned with the angular momentum axis L (small wobble angle). The magnetic axis continues to evolve until it is orthogonal to the angular momentum axis. The result is an oblate configuration that is optimal for GW emission.

4.2.1 Newly Born Magnetar Spindown

Both EM torques and GW emission torques draw from the magnetars rotational energy given by:

$$E_{rot} = \frac{1}{2} I \Omega^2 \tag{4.36}$$

We are interested in the spindown rate of the magnetar as a function of the wobble angle. To find an equation for the spindown rate we simply differentiate [4.36] with respect to time:

$$\dot{\Omega} = \frac{\dot{E}_{rot}}{I\Omega} \tag{4.37}$$

Where $\dot{E}_{rot}$ is the sum of luminosities due to GWs and EM radiation, $\dot{E}_{GW}$ and $\dot{E}_{EM}$. If we can calculate these luminosities as a function of a time dependent wobble angle, we can quantify the time scale for which GWs will remain detectable from a magnetar.

The GW luminosity emitted by a precessing magnetar is easily found by using [1.24] and substituting the third time derivative of the precessing bodies quadrupole tensor as a function of the wobble angle. The result is:

$$\dot{E}_{GW} = -\frac{2}{5}\frac{G(I\epsilon_B)^2}{c^5}\Omega^6 \sin^2(\theta_{wob})(1 + 15\sin^2\theta_{wob}) \tag{4.38}$$

The EM luminosity for the non-precessing case can be found in general by using the Larmor formula. The EM luminosity in the precessing case was calculated numerically by Spitkovsky [23]. The result was:

$$\dot{E}_{em} = \frac{2}{3}\frac{\mu^2\Omega^4}{c^3}(1 + \sin^2\theta_{wob}) \tag{4.39}$$

It is clear that for a small wobble angle, EM radiation is the dominant effect for depleting the magnetars rotational energy reservoir. Therefore, if the precession is damped or the stars remains in its prolate configuration, GWs will not be observable either because the star is frozen in its approximate axis-symmetric motion or because the wobble angle evolves slow enough such that the EM radiation depletes the stars rotational energy before the GWs can take over.

In short, the orthogonalization process, depicted in figure [4.1], must be quick enough for strong GW emission to ensue promptly, in order for it to be competitive with EM radiation!

Precisely how fast this orthogonalization process happens is equivalent to finding the time evolution of the wobble angle. This was calculated by Dall'Osso et al. [24]. The main ideas of this calculation are summarized in the next subsection.

4.2.2 Wobble Angle Evolution

An elastic prolate NS with a frozen-in magnetic field, as previously mentioned, is unstable. This is because the rotational energy of a rotating spheroid is minimized, at a fixed angular momentum, when its moment of inertia is maximum. For a prolate figure, this is achieved when the symmetry axis is orthogonal to the spin axis.

In the presence of internal dissipative processes, the magnetic axis of a prolate NS will be driven towards orthogonal rotation, in other words the wobble angle between the NS's angular momentum J_i and its magnetic axis n_B grow on a dissipation timescale until J_i and n_B are orthogonal. This configuration is the optimal one for GW emission.

There are in essence two competing mechanisms relevant to wobble angle evolution. One of these mechanisms damps the evolution while the other enhances the evolution. They are:

- The gravitational wave back reaction
- Viscous energy dissipation in the neutron star interior

Each of these mechanisms are discussed in detail below.

Gravitational Wave Back Reaction

GWs emission in fact damps the wobble angle evolution. To see why this is the case a quick derivation can be done. Firstly, the rotational energy [4.36] can be written in terms of the wobble angle, angular momentum and principle moments of inertia:

$$E_{rot} = \frac{L^2}{2}\left(\frac{\sin^2\theta_{wob}}{I_1} + \frac{\cos^2\theta_{wob}}{I_3}\right) \tag{4.40}$$

To find how GWs effect the wobble angle we need to take the time derivative of the equation above. To do this we need to find $\frac{dL}{dt}$, the time derivative of the angular momentum. This can easily be found using [1.25]. The result is:

$$\frac{dL}{dt} = -\frac{2G}{5c^5}(I_1 - I_3)^2\Omega^5 \sin^2\theta_{wob}(\cos^2\theta_{wob} + 16\sin^2\theta_{wob}) \tag{4.41}$$

Substituting this and taking the time derivative of [4.40] gives:

$$\dot{\theta}_{wob} = -\frac{2G}{5c^5}\frac{(I_1 - I_3)^2}{I_1}\Omega^4 \sin\theta_{wob}\cos\theta_{wob}(\cos^2\theta_{wob} + 16\sin^2\theta_{wob}) \tag{4.42}$$

Hence, we can see that GWs always drive the wobble angle to zero, meaning that the star will remain in its prolate, non-optimal GW emission configuration.

Viscosity Driven Energy Dissipation

In competition with the GW back reaction is internal viscosity driven energy dissipation that drives the wobble angle orthogonalization, causing the star to change from a prolate to an oblate configuration.

Internal viscous forces in the NBM interior drive an initially prolate configuration into an oblate configuration, optimal for GW emission, by precession energy dissipation.

The energy dissipation time scale is defined as:

$$\tau_{diss} \equiv \frac{2E_{pre}}{\dot{E}_{diss}} \tag{4.43}$$

And may be written in the following way as [25]:

$$\tau_{diss} = \frac{I}{\epsilon_B}\frac{1}{\int \xi \left(\frac{\Delta\rho}{\rho}\right)^2 dV} \tag{4.44}$$

Where ξ is the bulk viscosity of the NBM. According to Dall'Osso et al this can be re-expressed using dimensional analysis as [24]:

$$\tau_{diss} \sim \frac{2\rho R^2}{5\epsilon_B \epsilon_\Omega^2 \xi} \tag{4.45}$$

Where ϵ_Ω and ϵ_B are the axis symmetric deformation due to the magnetars own rotation and the deformation due to the magnetic field respectively.

We can see that the dissipation time is is inversely proportional to the bulk viscosity snd proportional to the magnetically induced ellipticity since $\xi \propto \epsilon_B^{-2}$. This means that for larger magnetically induced ellipticities, the dissipation time scale will grow and the magnetar will take longer to orthogonalize.

Dall' Osso et al. [26] showed that the time scale for wobble angle orthogonalization is related to the dissipation time scale by the simple relation:

$$\tau_{\theta_{w_{wob}}} = \tan^2 \theta_{wob} \tau_{diss} \tag{4.46}$$

The importance of orthogonalization in the early evolution of a newly formed magnetar can be determined by comparing this dissipation time-scale to the EM and GW spin-down time-scales.

Cutler 2002 [22] showed that the dissipation time scale is significantly faster than both the EM and GW emission time scales and gave an estimate for each. The dissipation time scale is shown below:

$$\tau_{diss} = \frac{1}{3 \times 10^{-8}} \left(\frac{n}{10^4}\right) \left(\frac{300Hz}{\Omega}\right) \left(\frac{10^{-7}}{\epsilon}\right) \tag{4.47}$$

The parameter n is related to the wobble period and is generally difficult to measure but can be up to a value of 10^9 before the dissipation time scale becomes longer than that for EM and GW emission.

In summary, there is strong evidence that the dissipation time scale is sufficiently small to ensure that magnetically deformed magnetars with toroidal fields will emit GWs. It is nonetheless important to understand that a search targeting a newly born magnetar may not detect GWs immediately at birth over this dissipation time scale before the body has time to orthogonalize.

Finally, it is worth noting that other mechanisms have been hypothesised to enhance this wobble angle evolution. For example, the core and crust will not wobble together rigidly, and relative internal motions will lead to frictional energy dissipation. This is contingent on prompt crust formation after birth. This is discussed briefly in section 4.2.4.

4.2.3 Magnetic Field Decay

Since the magnetic field is directly responsible for the magnetars ellipticity, we are interested in the potential scenario of magnetic field decay. If the magnetic field decay is significant during a time scale comparable to the GW observation time, it will alter the amplitude of the signal.

There are a variety of physical mechanisms that have been suggested as a cause for magnetic field decay including Ohmic decay, Hall evolution in the crust and ambipolar diffusion in the core. (see [27] for an overview).

Dall'Osso et al.[28] claims that there is significant evidence of magnetic field decay for magnetars with dipolar magnetic fields of order 10^{15}G but only on time scales of millennia. Therefore, for our analysis of NBMs we will no longer consider the possibility of a time varying ellipticity since our search proposal is aimed at systems that require observations over a time scale of only days.

4.2.4 Cooling

As mentioned, other mechanisms may cause faster precession damping, notably crust core coupling in which the core and crust will not wobble together rigidly, and relative internal motions will lead to frictional damping.

A caveat to this crust core interaction is the prompt formation of the crust and superfluid that occurs when the NS cools below a certain temperature. In particular these effects are thought to come from the coupling between superfluid neutrons in the core and relativistic electrons in the crust, described by [29].

If the NBM is absent of viscous mechanisms, the wobble angle will not evolve and EM radiation will be highly dominant, depleting the stars rotational energy, unless these crust core coupling effects take place. Therefore, in the hypothetical absence of viscous dissipation mechanisms, cooling must occur place on a time scale of days for GWs to be detectable as the star will not be orthoganalized in time!

The cooling mechanisms and corresponding timescales depend highly on the state of the highly dense matter inside the neutron star which controls the neutrino emission cooling as well as on the outer layers of the neutron star that control photon emission cooling. For an overview of cooling mechanisms see [30].

Generally speaking, for a neutron star made solely from protons, neutrons and electrons, there is a competition between two processes known as Direct Urca Cooling and Modified Urca Cooling.

Direct Urca Cooling is considered to be a fast process and can only take place if a certain threshold fraction of protons are present. Direct Urca cooling operates through beta decay and electron capture.

The Modified Urca cooling process is considered to be the main cooling process for neutron stars and has a temperature evolution given by Owen at al. [31]:

$$\frac{T(t)}{10^9 K} = \left[\frac{t}{\tau_c} + \left(\frac{10^9 K}{T_i} \right)^6 \right]^{-\frac{1}{6}} \tag{4.48}$$

We want the temperature to fall from $10^{10} K$, the temperature at birth, to $2 \times 10^9 K$, the temperature at which the crust is expected to form. According to [4.48], using typical values for $\tau_c = 1yr$ we get that the NS will take between 5-6 days to cool down sufficiently. Since this is on a time scale longer than our observation time, we will only consider the aforementioned internal viscous mechanisms as drivers for the wobble angle evolution.

Chapter 5

Results

The purpose of this chapter is to estimate the performance of our search for currently active and future generation GW detectors and discuss the effects and limitations of neutron star astrophysics on the practicality of the search.

5.1 Search Range

We now estimate the range of our search proposal for a variety of detectors by calculating the non-centrality parameter [3.22] that solves equation [3.17]. To do this we need the noise spectral density values for the detector that we wish to analyze.

Seen below are the noise curves for currently active GW detectors: Advanced Virgo and KAGRA and the planned next generation detectors, the Einstein Telescope and Cosmic Explorer, taken from the LIGO online public database [32]:

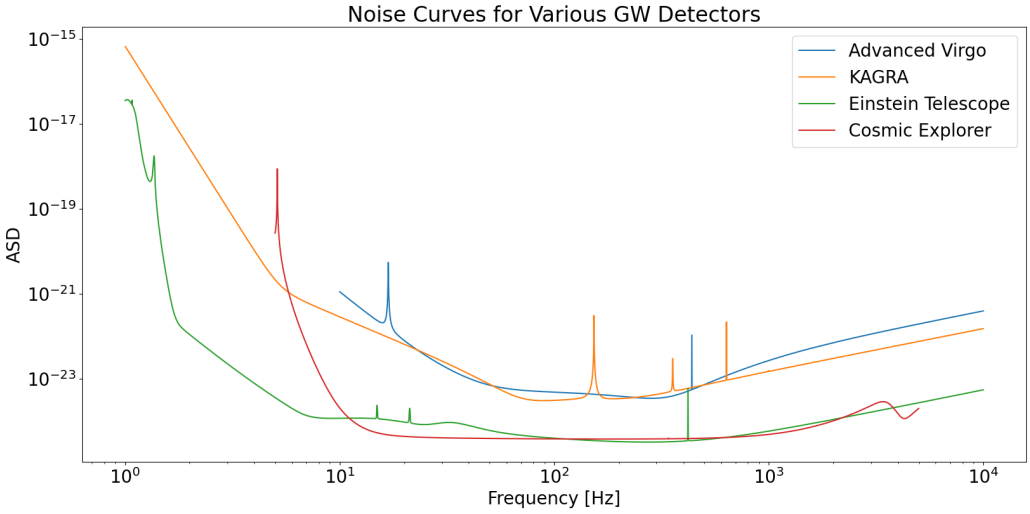

Figure 5.1: The noise amplitude spectral densities for a variety of GW detectors

To obtain the noise spectral density values $S_n(f_i)$ in equation [3.22] we simply square the amplitude spectral density values shown in figure [5.1]. In turn, the T_{sft} values are obtained using the condition [3.5].

We then calculated the threshold range, for our search method for Advanced Virgo, KAGRA, Cosmic Explorer and the Einstein Telescope following the logic explained in Chapter 3, using the Sympy, Scipy and numpy Python Packages. The Python script used for this calculation is appended to this thesis and can be found in Appendix B.

The results in kiloparsecs for Advanced Virgo and KAGRA are shown below in figure [5.2] for a 1.4 $M_{\odot}$ NS with a 10km radius and a magnetic field of 10^{15}G. For our frequency model we chose $f_0 = 1000Hz$, $\tau = 10000s$ and $n = 5$.

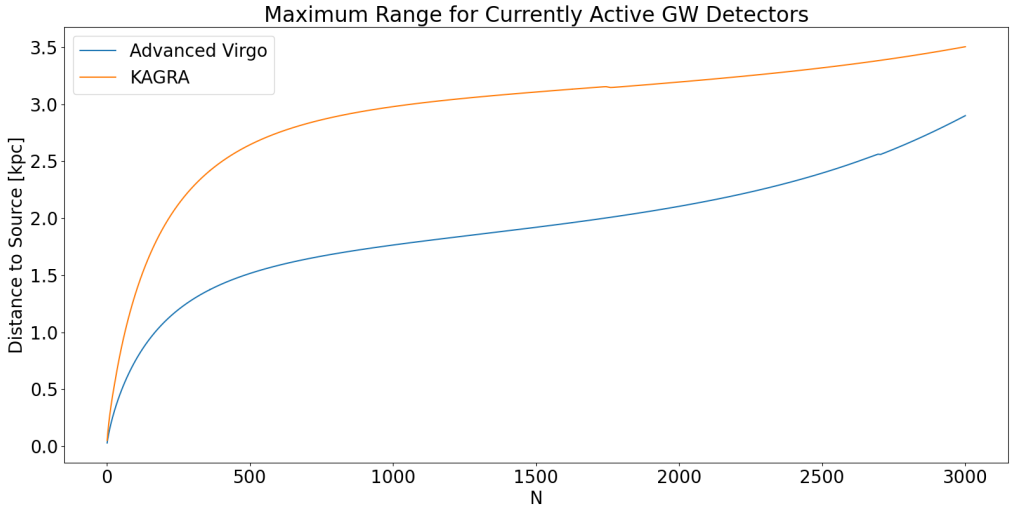

Figure 5.2: Maximum range in kiloparsecs for Advanced Virgo and KAGRA using our modified Stackslide search method for a Magnetar with 1.4 $M_{\odot}$, 10km radius and a magnetic field of 10^{15}G.

A few features of the above figure should be pointed out. Firstly, the range of the search increases sharply for the first 500 SFTs and increases gradually thereafter. Secondly, the range for Advanced Virgo and KAGRA decrease with N for $(1746 < N1760)$ and $(2694 < N < 2704)$ respectively. This corresponds to the peaks in the noise curves.

Overall, for an average NBM without taking any other effects into account, we expect our range to be roughly of the order of 10^{20} meters or roughly 3 kpcs for current GW detectors such as Advanced Virgo and KAGRA. For the next generation of GW detectors such as the Einstein Telescope, we can expect improvements by a factor of about 25 for observing a NS with the same parameters as before. (see figure [5.3]).

Note that these results are for the ideal case in which we are not considering the orthogonalization delay due to the finite dissipation time scale. Additionally we do not consider the depletion of the rotational energy due to EM radiation which would require a braking index ($n \neq 5$). These range calculations are thus for the optimal case. When actually performing the search a braking index range would be searched over in parameter space.

Finally, we point out that the value for the ellipticity due to the magnetars magnetic field that were derived in the previous chapter may differ greatly to the actual value. This point and its affect on the search range is discussed in detail in the next chapter.

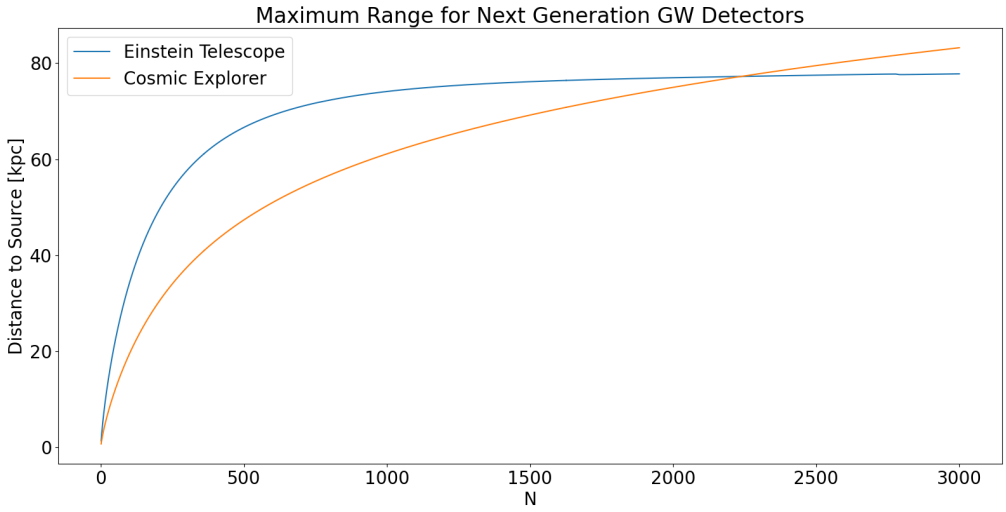

Figure 5.3: Maximum range in kiloparsecs for the Einstein Telescope and Cosmic Explorer using our modified Stackslide search method for a Magnetar with 1.4 $M_{\odot}$, 10km radius and a magnetic field of 10^{15}G

Chapter 6

Discussion

In this chapter we summarize our results and discuss the future work that can be done using the results found in this thesis. The next obvious step would be to actually perform a search using our modified Stackslide method. We take the opportunity in this chapter to describe how one would set-up this search and construct an appropriate parameter space to search over. Finally we end this chapter by giving a final word on the improvements that could be made to our NS models given that this search method will result in reliable detections in the future.

6.1 Search Range Implications

The main goal of this work was to propose a search for GWs from newly born magnetars. To do this we used a modified version of the Stackslide search method.

We found that under optimal conditions, where the issue of cooling, EM emission and dissipation time scales were ignored, that the maximum range for our search method is approximately 80 kpc for future generation GW detectors. While this is more than sufficient to cover our own galaxy, it falls far short of reaching the nearest neighbouring galaxy, the Andromeda galaxy. Considering the expected event rate of supernovae in our own galaxy is about 2/century, it is clear that search ranges of intergalactic scales is desirable. Furthermore, in reality the magnetar will take a finite amount of time to orthogonalize, giving EM torques an opportunity to deplete the stars rotational energy, meaning that our range estimates here are certainly idealistic. With these caveats in mind, we still believe that this search is worth performing.

Another point of discussion, as previously mentioned, is the fact that the ellipticity of the magnetar is a generally largely unknown value in practice and as we have shown in chapter 4, it is highly contingent on the NS model that we are using. Since the NS model that we are using in this thesis contains many simplifications (see below), it is conceivable that the ellipticity may vary significantly to the value that we use in this thesis. Furthermore, the range of the search varies linearly with the ellipticity. We can therefore make the following assertion: For our search range to reach the Andromeda galaxy (at 780 kpc) for future generation GW detectors, our ellipticity would need to be about an order of magnitude larger ($\approx 10^{-4}$ for a NS with the same parameters used in the results section). This is an order of magnitude above the supposed upper limit of 10^{-5} for NSs made of normal matter [33] but may lie below the upper limit of NSs made of more exotic matter [34]. With even more sensitive detectors in the future, intergalactic search ranges may be obtainable.

6.2 Performing the Search

To actually perform the search we must construct the discretized parameter space to search over. We remind the reader that the whole purpose of our search proposal was to attempt to by-pass the F-statistic approach which would require approximately 16 spindown parameters [3.1] and therefore a corresponding parameter

space of at least 16 dimensions. In our proposal we use the analytic expression for our frequency model [2.20] and thus we are dealing with a more computationally manageable parameter space of only three dimensions, corresponding to our three unknown parameters $(n, \tau, f_{GW,0})$.

To construct the parameter space we must decide both the range over which to search and the resolution (spacing) between each discretized point. Once this is decided we construct the SFT segments for each template and sum the power in each SFT as described in detail in the previous chapters.

The range of each parameter can be determined by using astrophysical arguments. A reasonable search range for the braking index is $3 < n < 5$ which corresponds to the lower limit of pure EM dipole radiation and the upper limit of pure GW emission. For the initial frequency a search range of $0Hz < f_{GW,0} < 1000Hz$ is reasonable since NSs are expected to have a maximum spin frequency of approximately 500Hz. Finally, the boundaries for the parameter τ can be determined by combining equations [2.16] and [2.18] to get:

$$\tau = -\frac{1}{n-1}\frac{\Omega}{\dot{\Omega}} \tag{6.1}$$

Using reasonable value for the spin frequency, spindown and braking index, a reasonable range for τ should be $5000s < \tau < 50000s$.

To perform a comprehensive parameter space search, we must construct a grid that ensures that templates do not deviate from each other by at most one frequency bin over a duration the entire T_{obs} as ensured by the quarter cycle criterion [3.3]. The step sizes between each point in parameter space is then constructed in the following way [14]:

$$\delta n = \left.\frac{\partial n}{\partial f_{GW}(t)}\right|_{t=T_{obs}} \delta f \tag{6.2}$$

$$\delta \tau = \left.\frac{\partial \tau}{\partial f_{GW}(t)}\right|_{t=T_{obs}} \delta f \tag{6.3}$$

$$\delta f_{GW,0} = \left.\frac{\partial f_{GW,0}}{\partial f_{GW}(t)}\right|_{t=T_{obs}} \delta f \tag{6.4}$$

Where $\delta f = \frac{1}{T_{SFT}}$ in our case.

It will also be necessary to pad the earlier shorter duration SFTs with zeroes in order to artificially inflate their length to match the longest SFT segment in order to ensure that the frequency resolution does not change from one SFT to another.

A final point of discussion for the performance of the search itself is to point out that there are options to conceivably optimize this search method. An obvious way to do this is by including weights. We could for example, decide ahead of time which segments of the signal are subject to more noise relative to other segments and then use some criteria to determine mathematical weights that may be applied to individual segments such that segments that are subject to a lot of noise are weighted less and segments with less noise are weighted more. This will potentially improve the range of our search.

6.3 Neutron Star Modelling

The neutron star models that we considered in this thesis are quite basic. We used a rather simplistic barotropic equation of state. More realistic equations of state that depend on other parameters such as the temperature are more accurate to describing real neutron stars and could be considered in an analysis such as this. In addition, we also did not consider the effects of accretion or the magnetars external magnetic fields in its magnetosphere. Furthermore we only considered deformations resulting from the magnetars magnetic field and did not consider other modes of deformation nor did we consider the possibility of glitches, or semi-permanent crustal deformations.

It is clear that with reliable search methods for continuous GW signals, theoretical neutron star structure models may be confirmed or ruled out based purely on the Gravitational waveform since the waveform is highly dependent on the ellipticity, rotational frequency and orientation of the neutron star itself. The ellipticity itself is highly dependent on the density profile of the neutron star and so GWs from such bodies may act as a probe to the internal structure of the star.

It is without doubt that the reliable and consistent detection of gravitational waves from isolated bodies using our own search proposal or otherwise, will vastly improve our knowledge of both neutron star astrophysics and the structure of our own galaxy and beyond.

Appendix A

Calculation of Ellipticity for an n=1 Polytrope

In this appendix we go through the calculation of the ellipticity for an n=1 polytope.

We begin with the definition of the ellipticity [1.14] and re-write it here for convenience:

$$\epsilon = \frac{I_{zz} - I_{xx}}{I_0} \tag{A.1}$$

First we deal with the numerator and write it explicitly using the definition of the inertia tensor:

$$\begin{aligned} I_{zz} - I_{xx} &= \int_V \rho(r,\theta)(x^2+y^2)dV - \int_V \rho(r,\theta)(y^2+z^2)dV \\ &= \int_V \rho(r,\theta)(x^2-z^2)dV \end{aligned} \tag{A.2}$$

According to our assumption, we can write the density as a radial dependent spherically symmetric function plus a perturbation given by [4.21]. We will also only consider l=2 deformations, and so:

$$I_{zz} - I_{xx} = \int_V (\rho(r) + \delta\rho(r)P_{l=2})(x^2-z^2)dV \tag{A.3}$$

The spherical part will vanish:

$$I_{zz} - I_{xx} = \int_V \delta\rho(r)P_{l=2}(x^2-z^2)dV \tag{A.4}$$

We are only interested in terms that are of linear order in the deformation, e. Keeping in mind that the term $\delta\rho$ is already first order in the deformation, we may write our integral in spherical coordinates:

$$\int_0^{2\pi}\int_0^{\pi}\int_0^{R} \delta\rho(r)P_{l=2}(r^2\cos^2\phi\sin^2\theta - r^2\cos^2\theta)r^2\sin\theta dr d\theta d\phi \tag{A.5}$$

Plugging in the explicit expression for the Legendre polynomial ($P_{l=2} = \frac{1}{2}(3\cos^2\theta - 1)$) and carrying out the angular integrations gives:

$$I_{zz} - I_{xx} = -\frac{8}{30}(1+\pi)\int_0^R \delta\rho r^4 dr \tag{A.6}$$

Then substituting our expressions for $\delta\Phi$ [4.34] and $\delta\rho$ [4.33] gives the full explicit expression for the numerator of the ellipticity definition, $I_{zz} - I_{xx}$:

$$-\frac{8}{30}(1+\pi)\int_0^R \left[\frac{-r^4}{24R^2\rho_c G\pi^2}\left[6\pi^3\rho_c\left[\frac{-B^2}{36\pi^3\rho_c y^3}[(y^5-15\pi^2 y)\cos y + 5\pi^2(3-y^2)\sin y] - \frac{B^2\pi r}{R}\sin y\right]\right]\right] dr \tag{A.7}$$

The only step left to complete is to calculate the integral. The result is:

$$I_{zz} - I_{xx} = \frac{B^2(1+\pi)(\pi^2-15)R^3}{108\rho_c G\pi^4} \tag{A.8}$$

For the denominator, I_0, we simply need to find the inertia of the non-perturbed spherical star. For a non constant density star for which the density depends solely on the radius, the inertia is given by:

$$I_0 = \frac{8\pi}{3}\int_0^R \rho_c \frac{\sin y}{y} r^4 dr \tag{A.9}$$

Where the angular components of the integration have already been calculated and the polytropic density profile has been used.

The integral then yields:

$$I_0 = (\pi^2 - 6)\frac{R^5}{\pi^4\rho_c} \tag{A.10}$$

Combining [A.10] and [A.8] gives the following expression for the ellipticity:

$$\epsilon = \frac{B^2(1+\pi)(\pi^2-15)}{108\rho_c^2 R^2} \tag{A.11}$$

It is instructive to re-express the central density in terms of the body's mass:

$$M = \int_V \rho_c \frac{\sin y}{y} dV \tag{A.12}$$

Which gives the following expression for the central density:

$$\rho_c = \frac{M\pi}{4R^3} \tag{A.13}$$

Plugging this into the ellipticity gives:

$$\epsilon = \frac{27B^2R^4(1+\pi)(\pi^2-15)}{4M^2G\pi^2} \tag{A.14}$$

Which written in a more informative way can be expressed as:

$$\boxed{\epsilon \approx -1\times 10^{-11}\left(\frac{R}{10km}\right)^4\left(\frac{M}{1.4M_\odot}\right)^{-2}\left(\frac{\bar{B}}{10^{12}G}\right)^2} \tag{A.15}$$

Appendix B

Python Script for Range Calculation

Here we give the Python3 script used to calculate the range of our search method for the advanced Virgo detector.

```
# The point of this script is to calculate the depth at which this search can reach

# Importing necessary packages
from sympy import *
import numpy as np
import matplotlib.pyplot as plt
import scipy.constants as const
from scipy.stats import chi2
from scipy.optimize import curve_fit
from scipy.stats import ncx2
from scipy.optimize import fsolve

# Load Advanced Virgo Noise Curve
data = np.loadtxt("curves_Jan_2020/advirgo.txt")

#Load Tsft times found earlier
Tsft = np.loadtxt("Tsft_values.txt")
x, y, z = symbols("x y z")


# Define ellipticity
def ellip(R, M, B):
    e = ((1*10**-11)*((R/10)**4)*((M/1.4)**-2)*(B/10**12)**2)
    return e

# Define wave amplitude without 1/r
def amp(f):
    return (4*((np.pi)**2) * const.G * ellip(10,1.4,10**15) * (0.4 * 1.4*1.99*(10**30)

    * (10000)**2) * f**2)/(((const.c)**4))

# Frequency Model
def freq(t):
    return 1000*(t/10000 + 1)**(-1/4)
```

```
# Calculate frequency values at each SFT
freq_values = []
x = 0
for i in Tsft:
    freq_values.append(freq(i+x))
    x = x + i

# Amplitude values
amp_values = []
for i in freq_values:
    amp_values.append(amp(i))


# Interpolate noise values from Advanced Virgo noise curve data
Sn_values= []
for i in np.linspace(1000, 375.4484140608662, 3000):
    Sn_values.append(np.interp(i,data[:, 0], data[:,1]))

# Non-Centrality parameter
def lamda(T,S,H):
    return 7/64*(T/S)*(H**2)

# Evaluate and sum the non-centrality parameter in each SFT
lamda_values = []
sum_values = []
for i in range(3000):
     lamda_values.append(lamda(Tsft[i], np.square(Sn_values[i]) ,amp_values[i]))

     sum = 0;
     for i in range(0, len(lamda_values)):
        sum = sum + lamda_values[i];
     sum_values.append(sum)

# Calculate the value that the sum of the non-centrality parameter
# should be to achieve detection
expected_lambda_values = []

for i in np.linspace(1,3000,3000):
    def func (x):

        return ncx2.ppf(0.1,2*i,x)-(2.08*i + 58.57)
    root = fsolve(func,1000)
    expected_lambda_values.append(root[0])


# Solve for the threshold range that will
#result in the non-centrality parameter being large enough
#such that detection is acheived
Solutions = []
for i in range(3000):

       Q = solve(sum_values[i]/z**2 - expected_lambda_values[i])
       Solutions.append(Q[0])
```

```
SOLUTIONS = np.absolute(Solutions)

# Plot Results
X = np.linspace(1,3000,3000)
plt.plot(X,SOLUTIONS)
plt.title("Maximum Range")
plt.xlabel("N")
plt.ylabel("Distance to Source [m]")
plt.legend(["Advanced Virgo"])
plt.show()
```

Bibliography

[1] B. P. Abbott et al. "Observation of Gravitational Waves from a Binary Black Hole Merger". In: *Physical Review Letters* 116.6 (Feb. 2016). DOI: 10.1103/physrevlett.116.061102. URL: https://doi.org/10.1103%2Fphysrevlett.116.061102.

[2] *Max Planck Institute for Gravitational Wave Physics*. URL: https://www.aei.mpg.de/continuouswaves.

[3] URL: https://cw.docs.ligo.org/public/.

[4] *Einstein@home*. URL: https://einsteinathome.org/.

[5] Brendan T. Reed, Alex Deibel, and C. J. Horowitz. "Modeling the Galactic Neutron Star Population for Use in Continuous Gravitational-wave Searches". In: *The Astrophysical Journal* 921.1 (Nov. 2021), p. 89. DOI: 10.3847/1538-4357/ac1c04. URL: https://doi.org/10.3847%2F1538-4357%2Fac1c04.

[6] The LIGO Scientific Collaboration et al. *Searches for Gravitational Waves from Known Pulsars at Two Harmonics in the Second and Third LIGO-Virgo Observing Runs*. 2021. DOI: 10.48550/ARXIV.2111.13106. URL: https://arxiv.org/abs/2111.13106.

[7] Vladimir Dergachev and Maria Alessandra Papa. "Sensitivity Improvements in the Search for Periodic Gravitational Waves Using O1 LIGO Data". In: *Physical Review Letters* 123.10 (Sept. 2019). DOI: 10.1103/physrevlett.123.101101. URL: https://doi.org/10.1103%2Fphysrevlett.123.101101.

[8] Iraj Gholami Ghadikolaei. *Data analysis of continuous gravitational waves*. http://hdl.handle.net/11858/00-1735-0000-0001-30BF-9. Univ. Potsdam, 2008.

[9] Michele Maggiore. *Gravitational waves*. Oxford University Press, 2008.

[10] Lee S. Finn. "Detection, measurement, and gravitational radiation". In: *Physical Review D* 46.12 (Dec. 1992), pp. 5236–5249. DOI: 10.1103/physrevd.46.5236. URL: https://doi.org/10.1103%2Fphysrevd.46.5236.

[11] Piotr Jaranowski, Andrzej Kró lak, and Bernard F. Schutz. "Data analysis of gravitational-wave signals from spinning neutron stars: The signal and its detection". In: *Physical Review D* 58.6 (Aug. 1998). DOI: 10.1103/physrevd.58.063001. URL: https://doi.org/10.1103%2Fphysrevd.58.063001.

[12] Reinhard Prix and Badri Krishnan. "Targeted search for continuous gravitational waves: Bayesian versus maximum-likelihood statistics". In: *Classical and Quantum Gravity* 26.20 (Oct. 2009), p. 204013. DOI: 10.1088/0264-9381/26/20/204013. URL: https://doi.org/10.1088%2F0264-9381%2F26%2F20%2F204013.

[13] LIGO Scientific Collaboration. *LIGO Algorithm Library - LALSuite*. free software (GPL). 2018. DOI: 10.7935/GT1W-FZ16.

[14] Miquel Oliver, David Keitel, and Alicia M. Sintes. "Adaptive transient Hough method for long-duration gravitational wave transients". In: *Physical Review D* 99.10 (May 2019). DOI: 10.1103/physrevd.99.104067. URL: https://doi.org/10.1103%2Fphysrevd.99.104067.

[15] Stuart Louis Shapiro and Saul Arno Teukolsky. *Black holes, white dwarfs, and Neutron Stars: The physics of compact objects*. Wiley-VCH, 2004.

[16] Reinhard Prix. "Search for continuous gravitational waves: Metric of the multidetector $\mathcal{F}$-statistic". In: *Phys. Rev. D* 75 (2 Jan. 2007), p. 023004. DOI: 10.1103/PhysRevD.75.023004. URL: https://link.aps.org/doi/10.1103/PhysRevD.75.023004.

[17] Patrick R. Brady et al. "Searching for periodic sources with LIGO". In: *Physical Review D* 57.4 (Feb. 1998), pp. 2101–2116. DOI: 10.1103/physrevd.57.2101. URL: https://doi.org/10.1103%2Fphysrevd.57.2101.

[18] B Abbott et al. "All-sky search for periodic gravitational waves in LIGO S4 data". In: *Physical Review D* 77.2 (2008), p. 022001.

[19] I. W. Roxburgh. "Magnetostatic Equilibrium of Polytropes". In: *Monthly Notices of the Royal Astronomical Society* 132.2 (Apr. 1966), pp. 347–358. ISSN: 0035-8711. DOI: 10.1093/mnras/132.2.347. eprint: https://academic.oup.com/mnras/article-pdf/132/2/347/8075083/mnras132-0347.pdf. URL: https://doi.org/10.1093/mnras/132.2.347.

[20] Mina Zamani and Mohsen Bigdeli. "An analytic treatment of magnetically deformed neutron stars". In: *Astronomische Nachrichten* 342 (Apr. 2021). DOI: 10.1002/asna.202113862.

[21] B. Haskell et al. "Modelling magnetically deformed neutron stars". In: *Monthly Notices of the Royal Astronomical Society* 385.1 (Feb. 2008), pp. 531–542. DOI: 10.1111/j.1365-2966.2008.12861.x. URL: https://doi.org/10.1111%2Fj.1365-2966.2008.12861.x.

[22] Curt Cutler. "GWs from NSs with large toroidal mml:math xmlns:mml="http://www.w3.org/1998/Math/MathML" display="inline"mml:miB/mml:mi/mml:mathfields". In: *Physical Review D* 66.8 (Oct. 2002). DOI: 10.1103/physrevd.66.084025. URL: https://doi.org/10.1103%2Fphysrevd.66.084025.

[23] Anatoly Spitkovsky. "Time-dependent Force-free Pulsar Magnetospheres: Axisymmetric and Oblique Rotators". In: *The Astrophysical Journal* 648.1 (Aug. 2006), pp. L51–L54. DOI: 10.1086/507518. URL: https://doi.org/10.1086%2F507518.

[24] S Dall'Osso, L Stella, and C Palomba. "Neutron star bulk viscosity, 'spin-flip' and GW emission of newly born magnetars". In: *Monthly Notices of the Royal Astronomical Society* 480.1 (June 2018), pp. 1353–1362. DOI: 10.1093/mnras/sty1706. URL: https://doi.org/10.1093%2Fmnras%2Fsty1706.

[25] James R. Ipser and Lee Lindblom. "The Oscillations of Rapidly Rotating Newtonian Stellar Models. II. Dissipative Effects". In: 373 (May 1991), p. 213. DOI: 10.1086/170039.

[26] S Dall'Osso, Steven Neil Shore, and L Stella. "Early evolution of newly born magnetars with a strong toroidal field". In: *Monthly Notices of the Royal Astronomical Society* 398.4 (2009), pp. 1869–1885.

[27] Andrei P. Igoshev, Sergei B. Popov, and Rainer Hollerbach. *Evolution of neutron star magnetic fields*. 2021. DOI: 10.48550/ARXIV.2109.05584. URL: https://arxiv.org/abs/2109.05584.

[28] S. Dall'Osso, J. Granot, and T. Piran. "Magnetic field decay in neutron stars: from soft gamma repeaters to 'weak-field magnetars'". In: *Monthly Notices of the Royal Astronomical Society* 422.4 (Apr. 2012), pp. 2878–2903. DOI: 10.1111/j.1365-2966.2012.20612.x. URL: https://doi.org/10.1111%2Fj.1365-2966.2012.20612.x.

[29] MA Alpar and JA Sauls. "On the dynamical coupling between the superfluid interior and the crust of a neutron star". In: *The Astrophysical Journal* 327 (1988), pp. 723–725.

[30] Dany Page, Ulrich Geppert, and Fridolin Weber. "The cooling of compact stars". In: *Nuclear Physics A* 777 (Oct. 2006), pp. 497–530. DOI: 10.1016/j.nuclphysa.2005.09.019. URL: https://doi.org/10.1016%2Fj.nuclphysa.2005.09.019.

[31] Benjamin J. Owen et al. "Gravitational waves from hot young rapidly rotating neutron stars". In: *Phys. Rev. D* 58 (8 Sept. 1998), p. 084020. DOI: 10.1103/PhysRevD.58.084020. URL: https://link.aps.org/doi/10.1103/PhysRevD.58.084020.

[32] *LIGOnbsp;documentnbsp;T1500293-V13*. URL: https://dcc.ligo.org/LIGO-T1500293/public.

[33] Yuanhao Zhang et al. "Search for Continuous Gravitational Waves from Scorpius X-1 in LIGO O2 Data". In: *The Astrophysical Journal Letters* 906.2 (Jan. 2021), p. L14. DOI: 10.3847/2041-8213/abd256. URL: https://doi.org/10.3847/2041-8213/abd256.

[34] C. J. Horowitz and Kai Kadau. "Breaking Strain of Neutron Star Crust and Gravitational Waves". In: *Physical Review Letters* 102.19 (May 2009). DOI: 10.1103/physrevlett.102.191102. URL: https://doi.org/10.1103%5C%2Fphysrevlett.102.191102.